Air-Sea Exchange Drivers of Climate Variability, Ocean Circulation, and Weather: A Case For Coincident Observations of Ocean Surface Winds and Currents

Authors:
Ernesto Rodriguez, Jet Propulsion Laboratory, California Institute of Technology
Dudley Chelton, Oregon State University
Dmitry Dukhovskoy, Florida State University
Tom Farrar, Woods Hole Oceanographic Institution
M. Mar Flexas, California Institute of Technology
Thomas Kilpatrick, University of California, San Diego
Patrice Klein, IFREMER
Xinfeng Liang, University of South Florida, College of Marine Science
David G. Long, Brigham Young University
Nikolai Maximenko, University of Hawaii
Dimitris Menemenlis, Jet Propulsion Laboratory, California Institute of Technology
Steven L. Morey, Florida State University
Roger Samelson, Oregon State University
A. F. Thompson, California Institute of Technology
Shang-Ping Xie, University of California, San Diego

Supporters:
Abderrahim Bentamy, IFREMER
Kenneth H. Brink, Scientist Emeritus, Woods Hole Oceanographic Institution
Renato Castelao, University of Georgia
Paul Chang, NOAA/NESDIS/STAR
Bertrand Chapron, IFREMER
Eric Chassignet, Florida State University
Allan Clarke, Florida State University
Naoto Ebuchi, Institute of Low Temperature Science, Hokkaido University
Raffaele Ferrari, Massachusetts Institute of Technology
Melanie Fewings, University of Connecticut
Boris Galperin, College of Marine Science, University of South Florida
Semyon Grodsky, Department of Atmospheric and Oceanic Science, University of Maryland
David Halpern, Jet Propulsion Laboratory, California Institute of Technology
Heather Holbach, Florida State University
Svetla Hristova-Veleva, Jet Propulsion Laboratory, California Institute of Technology
Jordi Isern-Fontanet, Institut de Ciencies del Mar (CSIC), Barcelona, Spain
Zorana Jelenak, NOAA/NESDIS/STAR
W. Linwood Jones, Central Florida Remote Sensing Laboratory, University of Central Florida
Greg King, Institut de Ciencies del Mar (CSIC), Barcelona, Spain
A. D. Kirwan, Jr., University of Delaware
Jessica Kleiss, Lewis & Clark College
Tong (Tony) Lee, Jet Propulsion Laboratory, California Institute of Technology
W. Timothy Liu, Jet Propulsion Laboratory, California Institute of Technology
Alison M. Macdonald, Woods Hole Oceanographic Institution
Sharan Majumdar, University of Miami
Ralph F. Milliff, University of Colorado
David Moroni, Jet Propulsion Laboratory, California Institute of Technology
Alexis Mouche, IFREMER
William J. Plant, APL, University of Washington

Lucrezia Ricciardulli, Remote Sensing Systems
Hyodae Seo, Woods Hole Oceanographic Institution
Haruhisa Shimoda, Professor, Tokai University
Neville Smith, Co-Chair Tropical Pacific Observing System 2020 Steering Committee
Michael Spall, Department of Physical Oceanography, Woods Hole Oceanographic Institution
Janet Sprintall, co-chair of the Western Pacific Task Team for TPOS2020, Scripps Institution of Oceanography
Michael Steele, APL, University of Washington
Ad Stoffelen, KNMI (Royal Netherlands Meteorological Institute)
Joseph Turk, Jet Propulsion Laboratory, California Institute of Technology
David E. Weissman, Hofstra University
Frank Wentz, Remote Sensing Systems

Contents

1. Overview

Contemporaneous, global, collocated observations of ocean surface currents (including ageostrophic components) and surface winds or stress are technically achievable and poised to provide the next major step forward in understanding the dynamics of the upper ocean and its coupling to the atmosphere, thereby improving and constraining future models of climate variability and change. Observation of the total surface current vector is a new capability that will be useful globally for understanding ***climate variability and climate change***. These observations can be used to address climate research questions in the polar regions where there are relatively rapid changes in ice coverage, and in the tropics where the ocean effects on ***weather*** via atmospheric bridges have large impacts on humankind. Collocated vector stress and current observations can be used for a remarkably wide range of applications, including improved ***weather forecasts***.

Coupled ocean and atmosphere models, used for understanding and anticipating changes to the ***Earth's climate system***, require surface currents for accurate air/sea fluxes of energy, moisture, and CO_2. Surface currents are also needed for estimating and understanding transport within the ocean. The absence of direct global measurements of ocean surface currents and their dependence on local wind stress is a major gap in our quantitative knowledge of the ***global climate system***. The air-sea interface is a critical link in the ***Earth's climate system***; incomplete knowledge of the dynamics at this interface causes significant errors in the representation of horizontal and vertical mass transports in the upper ocean, and limits the accuracy of climate and seasonal forecast models.

2. Primary Science Applications and Targets

There are three primary science applications related to ***Climate Variability and Climate Change***. Ten other applications are also very briefly described.

2.1 Atmosphere/Ocean Coupling Science Target

2.1.1 Description of the science target

Research question: What are the global ocean surface currents and how are they related to local surface wind stress? What are the dominant near-surface mixing processes as a function of wind stress?

Knowledge of global ocean surface currents, their relation to local surface wind, and the associated processes that control the structure of the ocean surface boundary is essential for understanding and predicting ocean-atmosphere exchange and lateral transport in the upper ocean. This knowledge is also essential for a comprehensive *understanding of the Earth's climate system* [1,2,3,4,5,6]. The global relation between the surface wind and the speed and direction of wind-driven surface currents is unknown. Near-surface currents in state-of-the-art ocean models disagree with estimates from drifters (**Figs. 1, 2**). Theory and inferences from near-surface measurements suggest that strong velocity shear differences [1], comparable to the magnitude of the wind-driven current itself, likely often occur over the upper few meters of the ocean (**Fig. 3**). The opportunity to develop a comprehensive, quantitative understanding of the relationship between surface currents and local wind stress offers the promise of a major advance in understanding the physical mechanisms that control mixing, air-sea exchange, and lateral transport near the surface of the ocean. This understanding is critical for modeling and predicting the evolution of the Earth's climate system, and is important in many other contexts. A climate example is the role of surface currents in El Niño Southern Oscillation (ENSO), which is the largest ***climate variability*** signal in the Earth system [3,5]. These measurements will also have immediate practical applications for tracking and forecast of marine debris and pollutants and in marine search and rescue operations [1,2].

2.1.2 Utility of Measured Geophysical Variables

Contemporaneous, global, collocated measurements of total surface currents and surface winds or stress will provide (1) an entirely new science capability for the direct, data-based analysis of wind-forced, ageostrophic upper ocean dynamics; and (2) an entirely new observational dataset for constraining research and operational models of ocean circulation and climate. The wind-driven component of surface currents can be isolated directly by statistical correlation methods or by using independent geostrophic current observations, including those derived from synergistic altimeter surface topography measurements (SWOT, Jason-series). Surface drifting buoys drogued to follow currents at a 15m depth also provide information on the vertical shear, which can be used to determine which mixing processes dominate for various wind regimes.

2.2 Tropical Science Target

2.2.1 Description of the science target

Tropical upper oceans feature intense currents with strong vertical, lateral and temporal variations [3]. Sea surface temperature (SST) is strongly coupled with the atmosphere, creating ENSO and other

climate modes of global/regional impact [5]. Horizontal advection, upwelling, and turbulent vertical mixing are fundamentally important for SST variability in the equatorial oceans [7,8].

Research Goal: Understand the spatio-temporal variability and dynamical mechanisms for equatorial upwelling.

The strong current systems near the equator (**Fig. 4**) play a central role in ***interannual variability***, especially in the onset and evolution of El Niño. There are also weaker meridional-vertical overturning circulations on each side of the equator (**Fig. 4**), sometimes called the shallow meridional overturning circulation cells, that are important to global climate and biogeochemical cycles [9,10]. The divergence of the equatorial zonal and meridional surface currents drives equatorial upwelling, a critically important and poorly observed aspect of the ***climate system***. The largest mean upwelling rates in the world occur near the equator (**Fig. 5**), where cold water (<20°C) with high concentrations of nutrients and CO_2 are brought to the surface.

Equatorial currents exhibit strong variability and their measurements are extremely sparse (measured at a handful of fixed moorings and irregularly by ships). Even by combining all of the 85 available Acoustic Doppler Current Profiler (ADCP) measurements made from ships in the Pacific during 1991-1999, the stable estimate of the mean meridional circulation shown in **Fig. 4** could only be obtained by averaging over all longitudes east of the dateline (i.e., over more than 8000 km of longitude; [11]). The spatio-temporal variability and dynamical mechanisms for equatorial upwelling remain poorly understood and poorly constrained in climate models. Insufficient understanding of surface current dynamics in the equatorial oceans limits the accuracy of surface current estimates from altimeter observations. Global concurrent observations of surface current velocity and wind stress will enable new insights into upper ocean dynamics and upwelling in the tropical oceans.

2.2.2 Utility of Measured Geophysical Variables

Because of the small Coriolis effect in the tropics, large zonal currents may be accompanied by modest sea surface height anomalies marginally detectable from satellite altimetry (e.g., the Yoshida-Wyrtki Jet on the equator in response to rapid zonal-wind changes on intraseasonal to seasonal timescales ($\partial\eta/\partial x \sim 0$ but finite $\partial\eta/\partial y$; [12]) (**Fig. 6**). Thus, direct current measurements will greatly expand our ability to monitor equatorial ocean variability. The intense advection by intraseasonal Yoshida-Wyrtki jets rectifies on ***ENSO development*** [15], and is a major source of uncertainty in ***ENSO prediction***.

The present generation of of Intergovernmental Panel on Climate Change (IPCC) climate models suffer major long-standing biases in simulating key features of equatorial ocean dynamics and climate: the equatorial cold tongue in the mean state and El Niño warming both extend too far westward in the Pacific (**Fig. 7**; [14]); even larger biases in the simulated SST distribution in the equatorial Atlantic; and excessive SST variance in the eastern equatorial Indian Ocean related to the Indian Ocean dipole mode [15]. Such biases severely limit the skills of models in ***seasonal prediction*** and ***future climate projection***. For example, the balance among upwelling, thermocline displacement, and surface heat flux determines the zonal structure of equatorial Pacific warming in response to anthropogenic greenhouse effect [16], which in turn affects El Niño and its effects on North America [17]. Direct measurements of surface currents strengthen observational constraints on three-dimensional advection and mixing in the ocean, thereby contributing to improving climate models.

2.3 Polar Science Target

2.3.1 Description of the science target

Research questions: How does the sea ice drift and upper ocean circulation change under the current climate? What are the pathways and propagation/accumulation rate of surplus freshwater in the Arctic Ocean and Subpolar seas?

The relationship between winds, near-surface wind-driven ocean currents and climate variability is particularly evident in polar regions [4,18]. The Arctic Ocean is a large freshwater reservoir that has been increasing due to accelerated melting of ice and increasing runoff over the last two decades (**Figure 9**). The near-surface currents determine the distribution and pathways of freshwater within the Arctic Ocean, a prominent factor regulating ***climate variability*** of the Northern Hemisphere through the influence on thermohaline circulation in the Subpolar North Atlantic [19,20,21,22]. Accumulation and release of freshwater in the Arctic Ocean and freshwater fluxes to the North Atlantic are controlled by the large-scale atmospheric circulation [22] (**Fig. 8**). Being dominated by strong anticyclonic regime since 1997, the Arctic Ocean and particularly the Beaufort Gyre have accumulated an anomalously high volume of sea ice and liquid fresh water [23,24]. When released, this surplus fresh water may substantially influence

thermohaline processes in the subpolar region potentially impacting climate. The accelerating Greenland Ice Sheet mass loss also exerts a significant impact on thermohaline processes in the sub-Arctic seas. It remains unclear how, where, and on what timescales Greenland meltwater can impact convective regions [25]. IPCC models do not explicitly consider accelerating Greenland runoff in the climate simulations. Thus, it is of primary importance to monitor the sea ice drift and upper-ocean circulation in the Arctic region.

2.3.2 Utility of Measured Geophysical Variables

Freshwater accumulates in the surface layer and propagates in the Arctic Ocean and the sub-Arctic seas near the surface until it is mixed downward by haline and thermal convection. In the warm season, when river runoff and melting are greatest, Arctic shelves are the major contributor to the Arctic freshwater budget. During this time the surface is ice-free and the freshwater currents can be directly observed by satellites. Surface currents in the Subpolar North Atlantic can be observed year round. Therefore, observations of winds and surface currents will provide a great deal of information about freshwater transport by both large-scale and meso-scale circulations, including eddies. The latter is important for understanding lateral advection of freshwater from the boundary currents into the interior seas and convective regions. However, freshwater circulation carried by surface currents in the central Arctic cannot be directly observed by satellites due to the presence of sea ice. Instead, sea ice drift can be measured and used to determine the surface ocean currents. Thus, observations of the sea ice drift in the Arctic provide information about the upper ocean circulation [27,28].

2.4 Secondary Science Targets and Applications

2.4.1 Climate modeling and modes of variability: Upper-ocean dynamics and air-sea exchange are relevant to a broad array of ocean-atmosphere processes and modes of variability in the earth system [5; 29]. Climate models do not capture these well [14,26], and the surface currents and stress provide important constraints for tuning models and improving their representation of physical processes [29].

2.4.2 *Improved climate, seasonal, and weather forecasting models*: Winds observed by individual scatterometer have been found to have a large impact on assimilation in the European Center for Medium Range Weather Forecasts (ECMWF) (**Fig. 10**). Some modes of climate variability (§2.4.1) have useful predictability, related to winds and currents, that impacts ***weather*** and regional water availability and the ***Global Hydological Cycle*** and ***Marine & Terrestrial Ecosystems*** [30,5,3].

2.4.3 *Improved practical prediction of pollutant dispersal and marine debris*: Accurate surface current data are of particular importance for determining the fate and origin of debris [1] and biological organisms floating on or near the ocean surface [2], from *Sargassum* [31,32,33] (**Fig. 11**) to many coastal marine species that spawn offshore and whose larvae must reach coastal nursery habitat (e.g., [46]). Surface currents also move marine litter, which was recently identified by G7 [34,35] as one of most urgent global problems and whose patterns and pathways are still not well known [47].

2.4.4 *Glacial ice extent and sea ice extent*: Radar backscatter from snow and ice is particularly sensitive to the presence of liquid water due to melting. Precise calibration coupled with high resolution makes scatterometer measurements useful for melt/freeze delineation [36]. The contrast between ocean and sea ice backscatter enables mapping of sea ice extent. Due to the metamorphic processes occurring over its history, so-called multiyear ice (sea ice that has survived the melt season) has a higher sigma-0 and can be uniquely mapped (e.g., **Figs.** 12 **– 14**).

2.4.5 *Iceberg tracking*: Forced by winds and currents, icebergs represent major hazards to navigation, but are also critical to southern ocean biology via transport of freshwater and nutrients. Fertilization from these "biological islands" supports an ***extensive food chain*** from the smallest to the largest of organisms [**37**].

2.4.6 *Vegetation canopy biomass and vegetation health*: Although not designed for vegetation monitoring, scatterometers have shown the ability to provide global and long-term monitoring of vegetation phenology [41] as well as essential inputs in the monitoring of carbon stock in tropical regions [42,43].

2.4.7 Air/Sea exchange of energy, moisture, momentum and carbon: The ocean absorbs 93% of excess energy gained in the Earth system (**Fig. 15**) [48] and almost half the ***carbon*** that exits the atmosphere [49] (**Fig. 16**). Ocean evaporation accounts for over a third of the ***rainfall*** on land (i.e., ***weather***) and plays a large role in regional water availability and the ***global hydrological cycle*** and ***marine & terrestrial ecosystems***. These transports and fluxes are sensitive to winds and currents (**Fig. 17**).

2.4.8 Vertical motion and primary production: Surface vector stress and currents can be used to infer upwelling and mixing, which can be very important

for nutrient transport and hence primary productivity, which in turn is related to high levels of the ***marine ecosystem***.

2.4.9 ***Extreme Events:*** Extreme events in and over the open ocean or on the shoreline are almost always related to extreme winds [50]. While the most extreme winds are difficult to observe because heavy rain rates obscure the ocean surface, the winds around these events cover a much greater area and are extremely useful in ***modeling and forecasting extreme conditions***. These winds and currents contribute to extreme local sea levels associated with storm surge. Rogue waves occur when wind events interact with strong currents or eddies. Enhanced resolution wind field estimates (ultra-high resolution [UHR]) can improve the forecaster interpretation (**Fig. 18**).

3. Key Measurement Requirements

3.1 Temporal Sampling: Appropriate temporal sampling of winds is a major observational requirement [44]. A decade of spaceborne observations indicate that, at a minimum, an average of 1-2 observations per day are required for appropriate wind sampling. Simultaneous observations are desired to study wind and current coupling, but the wind sampling could be complemented by ongoing operational platforms such as EUMETSAT's ASCAT or ISRO's OSCAT.

Temporal sampling of surface currents drives the mission design. The time scales associated with the atmosphere-ocean coupling are on the order of 1-2 days at scales of 100-200 km, to resolve synoptic surface wind variability and the sub-inertial ocean response or weak-wind or deep-mixed-layer conditions. Tropical temporal scales are even slower. Sampling of polar phenomena, such as polar lows, drives the requirements at polar latitudes to several samples per day.

Care must be taken that wind-driven inertial motions not be aliased into the low-frequency signal. The period of inertial motions varies with latitude. For the tropical goals, the inertial period is long (e.g., 69 hours at 10^o latitude) and should not present a major sampling problem. However, the inertial period becomes shorter than one day above 30^o and appropriate sampling requires several observations per day. Current wide-swath radar scatterometers can achieve this sampling up to mid-latitudes, but it is possible that some of the inertial signals might alias at higher latitudes. At these latitudes, the use of models will provide a means for removing the inertial motion contributions. To demonstrate the feasibility of this approach, we have examined the coherence of *in situ* inertial current measurements with an internal-wave admitting global ocean simulation [56] driven by ECMWF atmospheric analysis. **Figure 19** shows that there is significant coherence between simulated and observed inertial currents, which suggests that the effects of aliasing of near-inertial currents could be reduced by modeling and removing the inertial signal.

3.2 Spatial Coverage: The selection of a high inclination orbit is driven by the need to sample the polar ocean. Most scatterometer missions are sun-synchronous (orbit inclination ~98°) which is sufficient to meet our goals. Other high-inclination non-sun-synchronous orbits in the range between 82^o-98^o, which may have better diurnal sampling, would also meet our observation requirements. An additional spatial coverage issue is the ability to gain synoptic views of the ocean circulation so that derivatives (such as vorticity) can be calculated and an assessment can be made of the temporal evolution of the two dimensional field. **Figure 20** presents a comparison of what would be observed by a wide swath measurement against the swath capabilities of the forthcoming NASA SWOT mission, underscoring the need for wide-swath coverage of currents.

3.3 Spatial Resolution: The spatial resolution of the measurements is driven by: 1) the need to compute spatial derivatives (e.g., wind stress curl); and 2) the need to resolve smaller circulation features (wind and current) that may appear at higher latitudes, especially in the polar oceans. High resolution is also required in the polar oceans to discriminate between ice and water and increase coverage. Based on previous scatterometer experience, these requirements imply the need for spatial resolution in the 5km-10km range, or about a factor of 2 improvement on the existing capabilities.

3.4 Measurement Accuracy: The accuracy requirements are driven by the atmosphere-ocean coupling target. Using classical Ekman and bulk mixed-layer models to characterize the ageostrophic surface current component, accuracy requirements on stress can be derived (**Fig. 21**). Requirements for the collocated wind or stress measurements are derived from experience with existing satellite scatterometer systems. Nominal requirements are 2 cm s^{-1} for ocean surface currents and 0.02 N m^{-2} for surface stress, with global coverage on space-time scales of 100 km and 1-2 days, to resolve synoptic surface wind variability and the sub-inertial ocean response. These nominal requirements support the resolution of smaller signals through additional space or time averaging, e.g., 1 cm s^{-1} on space-times scales of 200 km and 1-2 days.

Assuming that data are collected with 5 km spatial resolution (as above), the surface current measurement random error must be on the order of 0.5 ms^{-1} in order to achieve the desired performance at 100-200 km scales. A nominal wind performance of 1ms^{-1} on each wind vector component for winds speeds less than 20 ms^{-1}, which is comparable to what present day scatterometers can achieve, is sufficient to meet our other science targets. These requirements are also sufficient for sea ice tracking.

4. Likelihood of Successful Implementation

Our science goals require an instrument that can provide simultaneous measurements of winds and ocean surface currents. The measurement of ocean vector winds through radar scatterometers, such as NASA's Ku-band QuikSCAT or RapidScat, EUMETSAT's C-band ASCAT series, or ISRO's Ku-band OSCAT, is a mature technology. Scatterometers are relatively low power (~100W), low mass, high heritage radars that can be implemented at a modest cost. In the next decade both EUMETSAT and ISRO will likely continue to operate scatterometers that will complement the temporal sampling of winds from a wind-current mission.

Measurement of the component of the ocean surface velocity along the line of sight was first demonstrated by airborne radars using along-track interferometry (ATI) [52,53]. The surface current along the line of sight can be obtained, given the wind speed and direction, by removing the known phase speed of the resonant Bragg waves and short gravity wave contributions. The ATI technique has been demonstrated from space during the SRTM and TerraSAR-X missions [54,55,56]. ATI requires flying two large synthetic aperture radar (SAR) antennas in space, and, although it has been proposed for a long-term mission in the ESA WaveMill concept, its implementation is quite challenging.

Chapron et al. [57] realized that some surface current information could be obtained by using the Doppler anomalies in a single-antenna conventional SAR system. Using this technique, measurements of one component of the current has been demonstrated in variety of scenes, including the Gulf Stream [57] and the Aghulhas current [58] (**Figure 22**), among others. The last decade has also seen the maturing of the geophysical algorithms required to separate the current from the Bragg wave and large-scale wave motions (see, for instance [59]). Note that the Doppler concept also applies to tracking of sea ice, where greater radar brightness and no wave motion results in a more accurate measurement than over the ocean.

Although less demanding than ATI, achieving global coverage in one day with SAR-Doppler is challenging. Due to radar ambiguity limitations, typical wide-swath SARs are limited to swaths on the order of 200 km, with resulting global coverage limited to weekly, or longer, periods. In addition, global SAR ocean coverage data volume is very large, which is the reason that Doppler current retrievals have been limited to case studies. Finally, vector current measurements with a SAR require a two-beam antenna, which complicates the design.

Recently, two different approaches have been proposed that overcome the sampling limitations of SAR to achieve global simultaneous estimation of winds and currents. The first approach [60,61] uses the 1800 km swath pencil beam scatterometer configuration of QuikSCAT and OSCAT coupled with pulse bursts and onboard Doppler processing to measure winds and currents simultaneously. The demonstration of this concept has been funded by NASA's IIP program with an aircraft instrument (DopplerScatt). It will collect its first set of science data in September, 2016. Another concept, DopSCAT [62], marries Doppler estimation with the ASCAT architecture, which has about half the QuikSCAT swath, and is under review at EUMETSAT for potential integration into future evolutions of ASCAT. Both of these concepts would provide wide swath coverage, and simultaneous estimation of winds and currents meeting the requirements quoted above with minimal changes in the basic scatterometer architecture, mass, and power requirements, although better current measurement performance and coverage results when using a higher frequency (e.g., Ka-band) and pencil-beam scanning. In the past year, NASA's Jet Propulsion Laboratory (JPL) and ISRO's Space Application Center (SAC) have studied a joint implementation of a high resolution Doppler scatterometer using Ka-band for high accuracy currents and winds together with a Ku-band scatterometer for wind climate continuity and reduced rain contamination (**Figure 23**). The proposed implementation is capable of meeting the space-time sampling and accuracy requirements outlined above. The concept can be implemented with currently available technology and at a cost consistent with existing scatterometers. ISRO has interest in a continued collaboration with NASA in developing a higher capability instruments.

References

[1] Maximenko, N., L. Centurioni, Y. Chao, K. Dohan, F. Galgani, B. D. Hardesty, K. L. Law, D. Moller, E. van Sebille, and C. Wilcox, 2015: Remote sensing of marine debris, Earth Science and Applications from Space (ESAS 2017) RF#1 white paper.

[2] Morey, S.L., N. Maximenko, and M. A. Bourassa, 2015: Satellite Measurements of Ocean Surface Currents – Critical Applications. Response to Decadal Survey RFI#1.

[3] Farrar, T., L. W. O'Neill, N. Smith and M. A. Bourassa, 2015: TPOS2020: An integrated observing system for 2020 and beyond. Response to Decadal Survey RFI#1.

[4] Dukhovskoy, D., M. A. Bourassa, 2015: Changing Arctic Climate System: Causes, Consequences, and Relationship to the Global Climate. Response to Decadal Survey RFI#1.

[5] Bourassa, M.A., S. L. Morey, S.-P. Xie, D. Chelton, R. Samuelson, T. Farrar, N. Maximenko and A. Thompson, 2015: Wind and Current Coupling. Response to Decadal Survey RFI#1.

[6] Chelton, D., J. T. Farrar, R. M. Samelson, 2015: Wind-driven Near-surface Vertical Motion in the Ocean. Response to Decadal Survey RFI#1.

[7] Wang, W., M.J. McPhaden, 2000: The surface layer heat balance in the equatorial Pacific Ocean. Part II: Interannual variability. *J. Phys. Oceanogr.*, **30**, 2989-3008.

[8] Wang, W. and M.J. McPhaden, 2001: The surface layer heat balance in the equatorial Pacific Ocean during the 1997-98 El Nino and 1998-99 La Nina. *J. Climate*, **14**, 3393-3407.

[9] McPhaden, M.J. and D. Zhang, 2002: Slowdown of the meridional overturning circulation in the upper Pacific Ocean. *Nature*, **415**, 603-608, doi: 10.1038/415603a.

[10] Chavez, F.P., P.G. Strutton, G.E. Friederich, R.A. Feely, G.C. Feldman, D.G. Foley, and M.J. McPhaden: 1999; Biological and Chemical Response of the Equatorial Pacific Ocean to the 1997-98 El Niño. *Science*, **286**(5447), 2126-2131, doi: 10.1126/science.286.5447.2126

[11] Johnson, G.C., M.J. McPhaden and E. Firing: 2001: Equatorial Pacific Ocean horizontal velocity, divergence, and upwelling. *J. Phys Oceanogr.*, **31**(3), 839-849.

[12] Nagura, M. and M. J. McPhaden,2010: Wyrtki Jet dynamics: Seasonal variability. *J. Geophys. Res.*, **115**, C07009, doi:10.1029/2009JC005922.

[13] Kessler, W.S. and R. Kleeman, 2000: Rectification of the Madden-Julian Oscillation into the ENSO cycle. *Journal of Climate*, **13** (20), 3560-3575.

[14] Flato, G., J. Marotzke, B. Abiodun, P. Braconnot, S.C. Chou, W. Collins, P. Cox, F. Driouech, S. Emori, V. Eyring, C. Forest, P. Gleckler, E. Guilyardi, C. Jakob, V. Kattsov, C. Reason, and M. Rummukainen, 2013: Evaluation of Climate Models. In: *Climate Change 2013: The Physical Science Basis*. Contribution of Working Group I to the Fifth Assessment Report of the Intergovernmental Panel on Climate Change [Stocker, T.F., D. Qin, G.-K. Plattner, M. Tignor, S.K. Allen, J. Boschung, A. Nauels, Y. Xia, V. Bex and P.M. Midgley (eds.)], Cambridge University Press, Cambridge, United Kingdom and New York, NY, USA, 741-866. http://www.climatechange2013.org/images/report/WG1AR5_Chapter09_FINAL.pdf

[15] Li, G., S.-P. Xie, and Y. Du, 2015: Monsoon-induced biases of climate models over the tropical Indian Ocean with implications for regional climate projection. *J. Climate*, **28**(8), 3058-3072, doi: 10.1175/JCLI-D-14-00740.1.

[16] DiNezio, P.N., A.C. Clement, G.A. Vecchi, B.J. Soden, B.J. Kirtman, and S.-K. Lee, 2009: Climate Response of the Equatorial Pacific to Global Warming. *J. Climate*, **22**(18), 4873-4892, doi: 10.1175/2009JCLI2982.1.

[17] Zhou, Z.-Q., S.-P. Xie, X.-T. Zheng, Q. Liu, and H. Wang, 2014: Global warming-induced changes in El Nino teleconnections over the North Pacific and North America. *J. Climate*, **27**, 9050-9064, doi:10.1175/jcli-d-14-00254.1.

[18] Pope, A., P. Wagner, R. Johnson, Jamie Shutler, Jenny Baeseman, and L. Newman, 2015: Community Review of Southern Ocean Satellite Data Needs. Response to Decadal Survey RFI#1.

[19] Proshutinsky, A., R.H. Bourke, and F. A. McLaughlin, 2002:, The role of the Beaufort Gyre in Arctic climate variability: Seasonal to decadal climate scales. *Geophys. Res. Lett.*, **29**(23), *2100, doi:10.1029/2002GL015847*.

[20] Dukhovskoy, D.S., M.A. Johnson, and A. Proshutinsky, 2004: Arctic decadal variability: An auto-oscillatory system of heat and fresh water exchange. Geophys. Res. Lett., **31**, doi:10.1029/2—3GL019023.

[21] Dukhovskoy, D.S. M. Johnson, and A. Proshutinsky, 2006: Arctic decadal variability from an idealized atmosphere-ice-ocean model. 2.

Simulation of decadal oscillations. *J. Geophys. Res.*, **111**, C06029, doi:10.1029/2004JC002820

[22] Proshutinsky, A., D. Dukhovskoy, M.-L. Timmermans, R. Krishfield, and J. Bamber, 2015: Arctic circulation regimes. *Discussion meeting issue 'Arctic sea ice reduction: the evidence, models and impacts (Part 2),'* D. Feltham, S. Bacon, M. Brandon and J. Hunt, eds., Philosophical Transactions Royal Society A, **373**(2052), doi:10.1098/rsta.2014.0160.

[23] Proshutinsky, A., R. Krishfield, M.-L.Timmermans, J. Toole, E. Carmack, F. McLaughlin,W. J.Williams, S. Zimmermann, M. Itoh, and K. Shimada, 2009: The Beaufort Gyre Fresh Water Reservoir: State and variability from observations. *J. Geophys. Res.*, **14**, C00A10, doi: 10.1029/2008JC005104.

[24] Haine, T.W.N., B. Curry, R. Gerdes, E. Hansend, M. Karcher, C. Lee, B. Rudels, G. Spreen, L. de Steur, K. D. Stewart, and R. Woodgate, 2015: Arctic freshwater export: Status, mechanisms, and prospects. *Global and Planetary Change*, **125**, 13-35, doi:10.1016/j.gloplacha.2014.11.013.

[25] Dukhovskoy, D.S., P.G. Myers, G. Platov, M.-L. Timmermans, B. Curry, A. Proshutinsky, J.L. Bamber, E. Chassignet, X. Hu, C.M. Lee, and R. Somavilla, 2016; Greenland freshwater pathways in the sub-Arctic Seas from model experiments with passive tracers. *J. Geophys. Res.*, 121, 877–907, doi:10.1002/2015JC011290

[26] Bellenger, H., É. Guilyardi, J. Leloup, M. Lengaigne, and J. Vialard, 2014: ENSO representation in climate models: from CMIP3 to CMIP5. *Climate Dynamics,* **42**(7), 1999-2018, doi:10.1007/s00382-013-1783-z.

[27] Steele, M., J. Zhang, D. Rothrock, and H. Stern, 1997: The force balance of sea ice in a numerical model of the Arctic Ocean. *Journal of Geophysical Research*, **102**(C9):21061-21079, *doi:*10.1029/97JC01454.

[28] Kimura, N. and M. Wakatsuchi, 2000: Relationship between sea-ice motion and geostrophic wind in the Northern Hemisphere. *Geophysical Research Letters*, **27**(22):3735–3738, doi:10.1029/2000GL011495.

[29] Muscarella, P. et al, 2015: Do Assimilated Drifter Velocities Improve Lagrangian Predictability in an Operational Ocean Model? *Mon. Wea. Rev.*, **143**, 1822-1832, doi:10.1175/MWR-D-14-00164.1

[30] Adams, R. M., K. J. Bryant, B. A. McCarl, D. M. Legler, J. O'Brien, A. Solow, and R. Weiler, 1995: Value of improved long-range weather information. *Contemporary Economic Policy*, **13**(3), 10-19, doi:10.1111/j.1465-7287.1995.tb00720.x.

[31] Gower, J.F.R. and S. A. King, 2011: Distribution of floating *Sargassum* in the Gulf of Mexico and the Atlantic Ocean mapped using MERIS. *Int J Remote Sens.,* 7, 1917-1929, doi:10.1080/01431161003639660.

[32] Gower, J., E. Young, and S. King, 2013: Satellite images suggest a new *Sargasssum* source region in 2011. *Remote Sensing Letters*, **4**(8), 764-773, doi:10.1080/2150704x.2013.796433.

[33] Gavio, B., M. Natalia Rincon-Diaz, and A. Santos-Martinez, 2015: Massive quantities of pelagic Sargassum on the shores of San Andres Island, Southwestern Caribbean. *Acta Biológica Colombiana*, **20**(1), 239-241, doi:10.15446/abc.v20n1.46109.

[34] Communiqué Meeting of the G7 Ministers of Science Berlin, 8-9 October 2015 https://www.bmbf.de/files/English_version.pdf

[35] Thompson, R. and N. Maximenko, 2016: Plastic pollution of the marine environment*Future of the Ocean and its Seas: a non-governmental scientific perspective on seven marine research issues of G7 interest, Williamson, P., Smythe-Wright, D, and Burkill, P., Eds.,* ICSU-IAPSO-IUGG-SCOR, Paris, 12-18.

[36] Ulaby F., and D.G. Long, 2013: *Microwave Radar and Radiometric Remote Sensing*, Univ. Michigan Press, Ann Arbor, Michigan, 984 p.

[37] Vernet, M., K.L Smith Jr., A.O Cefarelli, J.J. Helly, R.S. Kaufmann, H. Lin, D.G. Long, A.E. Murry, B.H. Robison, H.A. Ruhl, T.J. Shaw, A.D. Sherman, J. Sprintall, G.R. Stephenson Jr., K.M. Stuart, and B.S. Twining, 2012: Islands of Ice: Influence of Free-Drifting Antarctic Icebergs on Pelagic Marine Ecosystems. *Oceanography*, 25(3), 38-39.

[38] Nghiem, S.V., K. Steffen, G. Neumann, and R. Huff, 2005: Mapping of ice layer extent and snow accumulation in the percolation zone of the Greenland ice sheet, Journal of Geophysical Research – Earth Surface, **110**, F02017.

[39] Nghiem, S. and W. Tsai, 2001:Global snow cover monitoring with spaceborne k_u-band scatterometer. IEEE *Transactions on Geoscience and Remote Sensing*, **39**(10), 2118–2134, doi:10.1109/36.957275.

[40] Hall, D.K., S. V. Nghiem, C. B. Schaaf, N. E. DiGirolamo, and G. Neumann, 2009: Evaluation of surface and near-surface melt characteristics on the Greenland ice sheet using MODIS and Quikscat data. Journal of Geophysical Research – Earth Surface, **114**, F04006, *doi:*10.1029/2009JF001287.

[41] Frolking, S., T. Milliman, K. McDonald, J. Kimball, M. Zhao, and M. Fahnestock, 2006: Evaluation of the seawinds scatterometer for regional monitoring of vegetation phenology, *Journal of Geophysical Research*, **111,** *D17302, doi:*10.1029/2005JD006588.

[42] Harris, N., S. Brown, S. Hagen, S. Saatchi, S. Petrova, W. Salas, M. Hansen, P. Potapov, and A. Lotsch, 2012: Baseline map of carbon emissions from deforestation in tropical regions, *Science*, **336**(6088), 1573–1576, doi:10.1126./science.1217962.

[43] Saatchi, S., N. Harris, S. Brown, M. Lefsky, E. Mitchard, W. Salas, B. Zutta, W. Buermann, S. Lewis, S. Hagen, et al., 2011: Benchmark map of forest carbon stocks in tropical regions across three continents, *Proceedings of the National Academy of Sciences*, **108**(24), 9899-9904, doi:10.1073/pnas.1019576108.

[44] Wentz, F., C. Mears, B. D. Santer, D. Chelton, M. Bourassa, R. Milliff, 2015: Continuity of Air-Sea Climate Variables. Response to Decadal Survey RFI#1.

[45] Rocha, C., T. Chereskin, S. Gille, and D. Menemenlis, 2016: Mesoscale to submesoscale wavenumber spectra in Drake Passage. *J. Phys. Oceanogr.*, 46, 601-620.

[46] Feng, M., N. Caputi, J. Penn, D. Slawinski, S. de Lestang, E. Weller, and A. Pearce, 2011: Ocean circulation, Stokes drift, and connectivity of western rock lobster (*Panulirus cygnus)* population. Canadian Journal of Fisheries and Aquatic Sciences, 2011, **68**(7), 1182-1196, doi:10.1139/F2011-065.

[47] van Sebille, E., C. Wilcox, L. Lebreton, N. Maximenko, B.D. Hardesty, et al, 2015: A global inventory of small floating plastic debris. *Environmental Research Letters,* **10**(12), 2015-12, doi: 10.1088/1748-9326/10/12/124006

[48] IPCC report. 2015: Ocean Observations. Intergovernmental Panel on Climate Change (IPCC), Geneva, Switzerland.

[49] Sabine and Tanhua, 2000: Estimation of anthropogenic CO2 inventories in the ocean. *Annual Reviews of Marine Science*, **2**, 175-198, doi:10.1146/annurev-marine-120308-080947.

[50]Vose, R. S. S. Applequist, M. A. Bourassa, S. C. Pryor, R. J. Barthelmie, B. Blanton, P. D. Bromirski, H. E. Brooks, A. T. DeGaetano, R. M. Dole, D. R. Easterling, R. E. Jensen, T. R. Karl, K. Klink, R. W. Katz, M. C. Kruk, K. E. Kunkel, M. C. MacCracken, T. C. Peterson, B. R. Thomas, X. L. Wang, J. E. Walsh, M. F. Wehner, D. J. Wuebbles, and R. S. Young, 2014: Monitoring and Understanding Changes in Extremes: Extratropical Storms, Winds, and Waves. *Bull. Amer. Meteor. Soc.*, **95**, 377-386. doi: 10.1175/BAMS-D-12-00162.1

[51] Large, W.G., and Yeager, S.G., 2009: The global climatology of an interannually varying air–sea flux data set. *Clim. Dyn.*, **33**, 341–364, doi: 10.1007/s00382-008-0441-3.

[52] Goldstein R., and H.A. Zebker, 1987: Interferometric radar measurement of ocean surface currents. *Nature*, 328, 707–709, doi:10.1038/328707a0.

[53] Goldstein, R., T. Barnett, and H. Zebker, 1989: Remote sensing of ocean currents. *Science*, **246**(4935), 1282–1285, doi:10.1126/science.246.4935.1282.

[54] Romeiser, R., H. Breit, M. Eineder, H. Runge, P. Flament, K. De Jong, and J. Vogelzang, 2005: Current measurements by SAR along-track interferometry from a space shuttle. *IEEE Transactions on Geoscience and Remote Sensing*, , **43**(10)), 2315–2324, doi: 10.1109/TGRS.2005.856116.

[55] Romeiser, R., S. Suchandt, H. Runge, U. Steinbrecher, and S. Grunler, 2010: First analysis of Terrasar-X along-track INSAR-derived current fields. *IEEE Transactions on Geoscience and Remote Sensing*, , **48**(2), 820–829, doi:10.1109/TGRS.2009.2030885.

[56] Romeiser, R., H. Runge, S. Suchandt, R. Kahle, C. Rossi, and P. S. Bell, 2013: Quality assessment of surface current fields from TerraSAR-X and Tandem-X along-track interferometry and Doppler centroid analysis. *IEEE Transactions on Geoscience and Remote Sensing,* **52**(5), 2759-2772, doi: 10.1109/TGRS.2013.2265659.

[57] Chapron, B., F. Collard, and F. Ardhuin, 2005: Direct measurements of ocean surface velocity from space: Interpretation and validation. *J. Geophys. Res.*, **110**, *C07008, doi:10.1029/2004JC002809*.

[58] Rouault, M., A. Mouche, F. Collard, J. Johannessen, and B. Chapron, 2010: Mapping the Agulhas current from space: An assessment of ASAR surface current velocities. *Journal of Geophysical Research*, 115, *C10026, doi:*10.1029/2009JC006050.

[59] Johannessen, J., B. Chapron, F. Collard, V. Kudryavtsev, A. Mouche, D. Akimov, and K. Dagestad, 2008: Direct ocean surface velocity measurements from space: Improved quantitative interpretation of Envisat ASAR observations. *Geophysical Research Letters*, 35, *L22608, doi:*10.1029/2008GL035709.

[60] E. Rodríguez, 2012: Wide swath simultaneous measurements of winds and ocean surface currents, in International Ocean Vector Winds Science Team Meeting, June 2012, http://tinyurl.com/jhhnakj.

[61] Bao, Q., X. Dong, D. Zhu, S. Lang, and X. Xu, 2015: The feasibility of ocean surface current measurement using pencil-beam rotating scatterometer. *IEEE Journal of Selected Topics in Applied Earth Observations and Remote Sensing*, **8**(7), 3441–3451, doi:10.1109/JSTARS.2015.2414451.

[62] Fois, F., P. Hoogeboom, F. Le Chevalier, A. Stoffelen, and A. Mouche, 2015: Dopscat: A mission concept for simultaneous measurements of marine winds and surface currents. Geophys. Res. Oceans, **120**, 7857–7879, *doi:*10.1002/2015JC011011.

[63] R. Romeiser, 2005: Current measurements by airborne along-track INSAR: Measuring technique and experimental results. *IEEE Journal of Oceanic Engineering*, **30**(3), 552–569, doi: 10.1109/JOE.2005.857508.

[64] Ekman, V. W., 1905: On the influence of the Earth's rotation on ocean currents. *Ark. Mat. Astron. Fys.*, **2**(11), 1-36.

[65] Large, W. G., J. C. McWilliams, and S. C. Doney, 1994: Oceanic vertical mixing: a review and a model with a nonlocal boundary layer parameterization. *Rev. Geophys.*, **32**(4), 363-403, *doi:*10.1029/94RG01872.

[66] Kudryavtsev, V., V. Shrira, V. Dulov, and V. Malinovsky, 2008: On the vertical structure of wind-driven sea currents. *J. Phys. Oceanogr.*, **38**(10), 2121-2144, doi:10.1175/2008JPO3883.1.

[67] K.M. Stuart and D.G. Long, 2011: Tracking large tabular icebergs using the SeaWinds Ku-band microwave scatterometer. *Deep-Sea Research Part II*, 58(11-12), 1285-1300, doi:10.1016/j.dsr2.2010.11.004.

[68] D.G. Long, J. Ballantyne, and C. Bertoia, 2002: Is the Number of Icebergs Really Increasing? *EOS Trans. American Geophysical Union*, **83**(42), 469-474, doi: 10.1029/2002EO000330.

[69] Proshutinsky, A. Y., and M. A. Johnson, 1997: Two circulation regimes of the wind-driven Arctic Ocean. *J. Geophys. Res.*, **102**(C6), 12,493-12,514, *doi:*10.1029/97JC00738.

[70] Moran, K., Backman, J., and Farrell, J.W., 2006: Deepwater drilling in the Arctic Ocean's permanent sea ice. In Backman, J., Moran, K., McInroy, D.B., Mayer, L.A., and the Expedition 302 Scientists, Proc. IODP, 302: Edinburgh (Integrated Ocean Drilling Program Management International, Inc.). doi:10.2204/ iodp.proc.302.106.2006

[71] Cardinali, C., 2009: Monitoring the observation impact on the short-range forecast. *Q. J. R. Meteorol. Soc.*, **135**, 239-250, doi:10.1002/qj.366.

6. Graphics

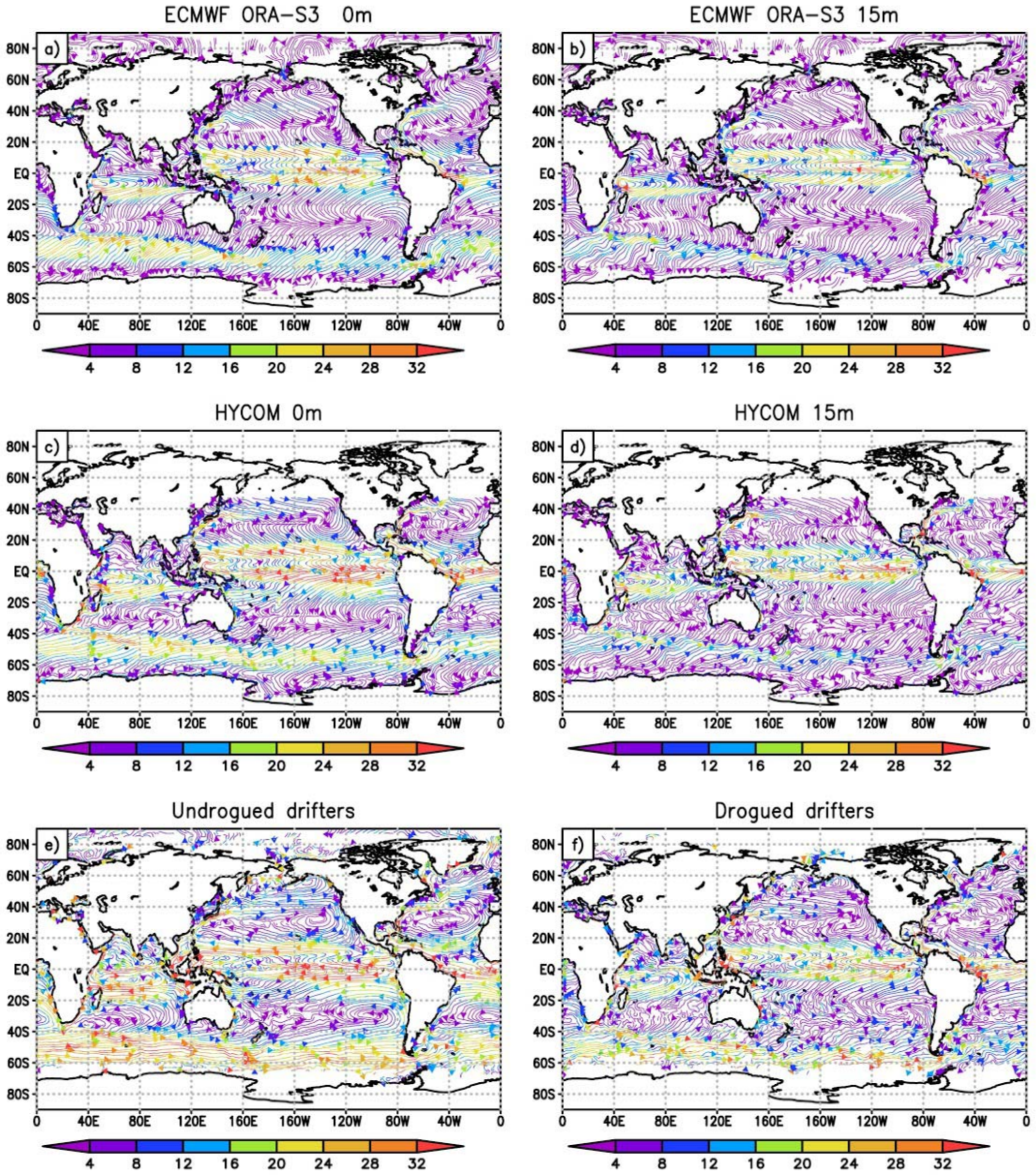

Figure 1: Streamlines of mean surface velocities (left column) and currents at 15 meters depth (right column), simulated in ECMWF (upper row), HYCOM (middle row) and measured by drifters (bottom row). Standard drifters are equipped with a six-meter-tall drogue, centered at 15 meters depth. After drogue is lost drifter continues sampling surface currents. Down-wind slip is not corrected here. Red shadow indicates speed and units are cm/s. Description, data and maps of the Global Drifter Program are available on http://www.aoml.noaa.gov/phod/dac/index.php

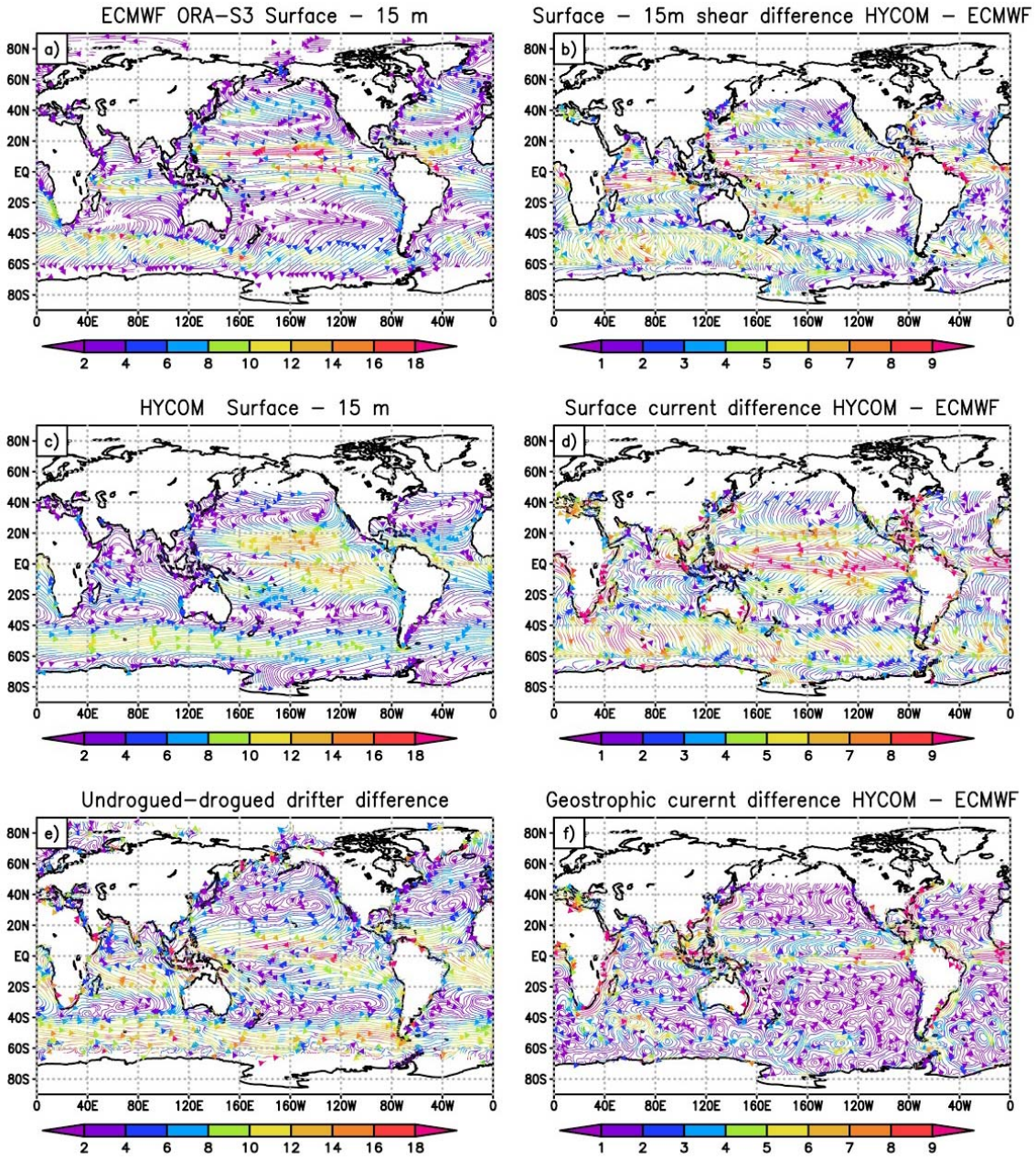

Figure 2: Mean velocity shear between the surface and 15 meters level in (a) ECMWF, (c) HYCOM and (e) drifter data. The model shear disagrees with drifter data and (b) between ECMWF and HYCOM. The latter disagreement is mainly due to the difference in surface currents (d). Differences in mean surface geostrophic velocities (f) are small and not organized, suggesting that most difficult for the models are wind-driven and other ageostrophic currents. Colors indicate the magnitude of the difference, units are cm/s.

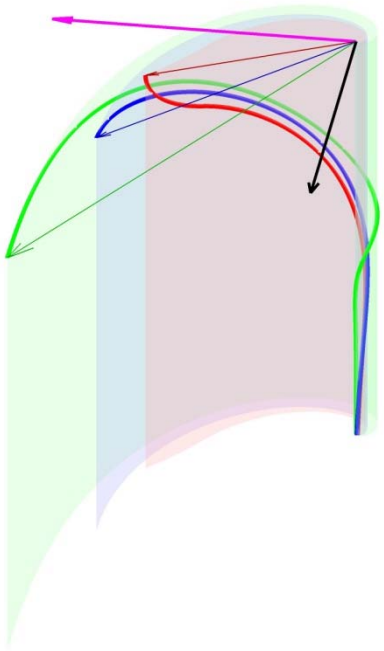

Figure 3: Near-surface velocity profiles of the wind-driven current for three conceptual models: classical Ekman spiral for constant viscosity (blue) [64], logarithmic boundary layer or KPP (green) [65] and momentum injection by breaking waves (red) [66]. Corresponding arrows show surface velocity vectors. Black arrow indicates wind stress and purple arrow is the depth-integrated Ekman transport (same to all models).

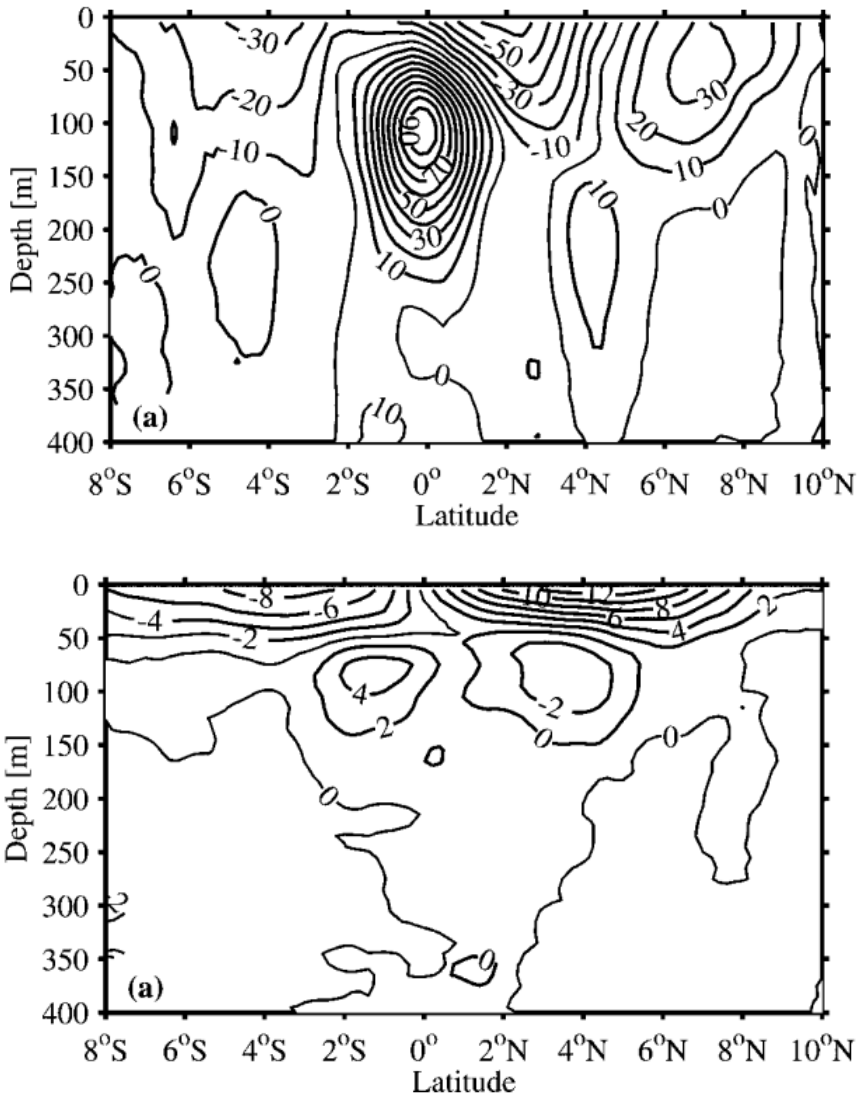

Figure 4: Estimates of latitude-depth profiles of zonal (top) and meridional (bottom) currents at 136°W (units of cm/s), constructed by averaging all 85 ADCP sections taken by ships between 95°W and 170°W during 1991-1999 [11]. The weaker mean meridional currents vary from about 10 cm/s to 0 cm/s over a distance of about 450 km.

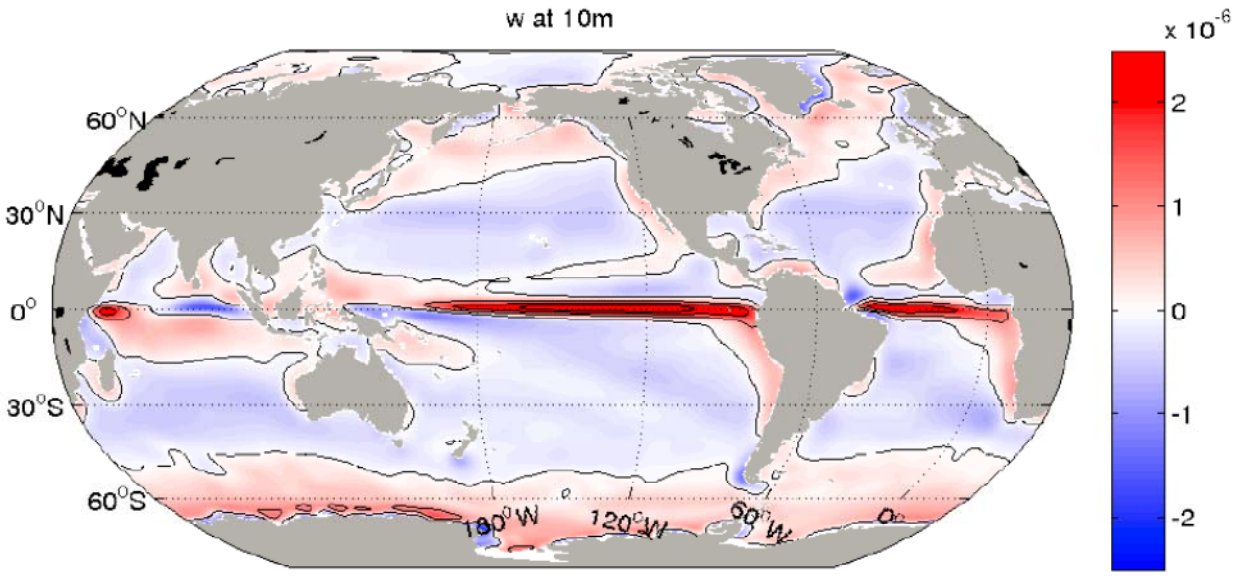

Figure 5: An estimate of the mean vertical velocity at 10 m depth (m/s; from from the ECCO V4 Ocean State Estimate; Liang et al., submitted). The largest mean vertical velocities are found in bands of intense upwelling on the equator.

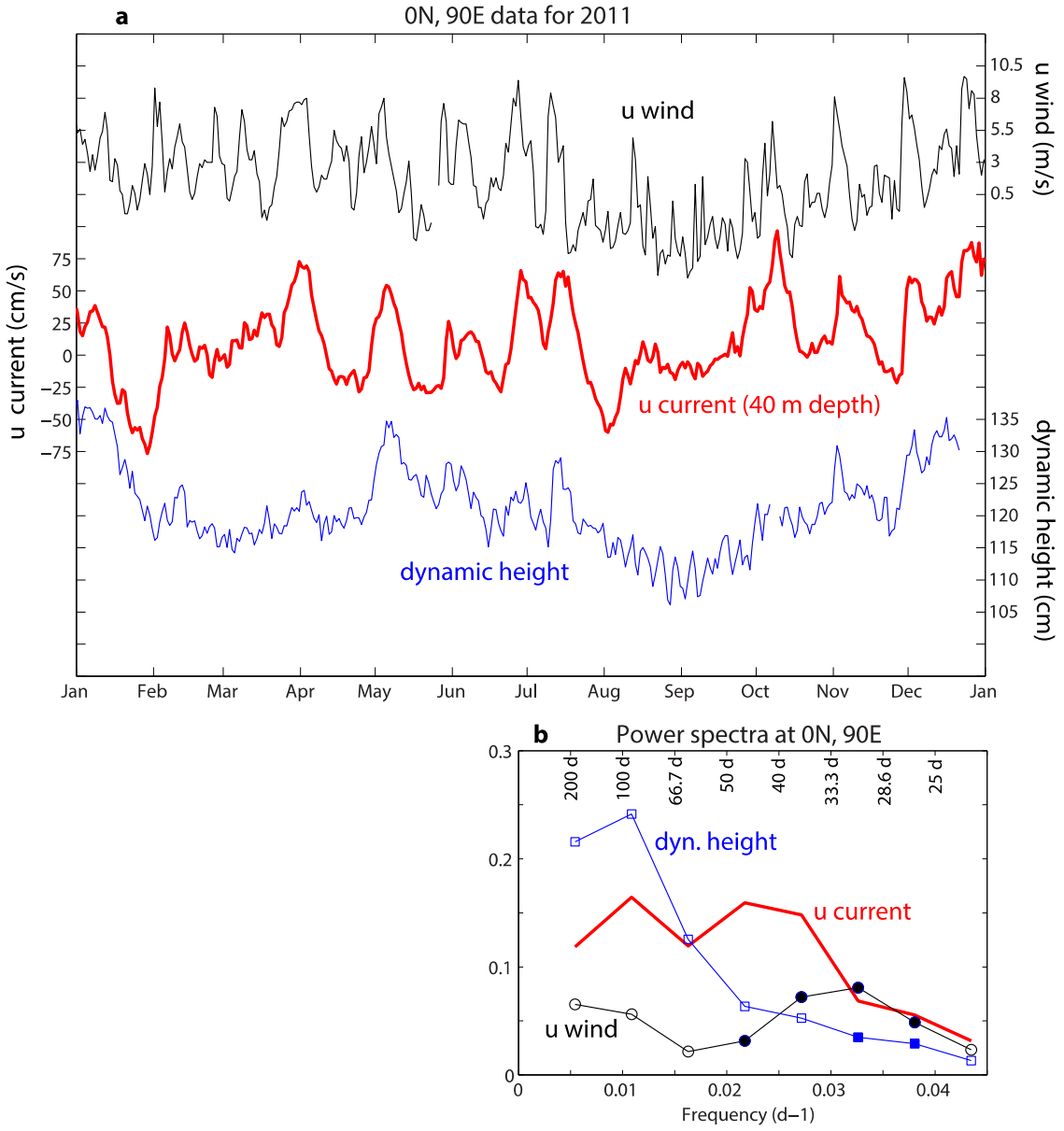

Figure 6 Top: Time series of zonal wind, zonal current 40 m depth, and dynamic height from the RAMA buoy at 0°N, 90°E, for 2011. Daily averaged data are shown. Note the strong variability in the zonal current at 30–50 days, with amplitudes of 50–100 cm/s. Several of the jets have a small or negligible signal in dynamic height. **Bottom-right**: Power spectra for zonal wind, zonal current at 40 m depth, and dynamic height. Filled circles/squares indicate coherence with the u current exceeds the 90% level. Note that zonal current features a 30-50-day peak, which is missing in dynamical height. While the coherence is high between zonal current and local zonal wind at the 30-50-day peak, the coherence is low between zonal current and dynamical height at both the 30-50 and 90-day peaks, illustrating the importance for direct observations of surface currents.

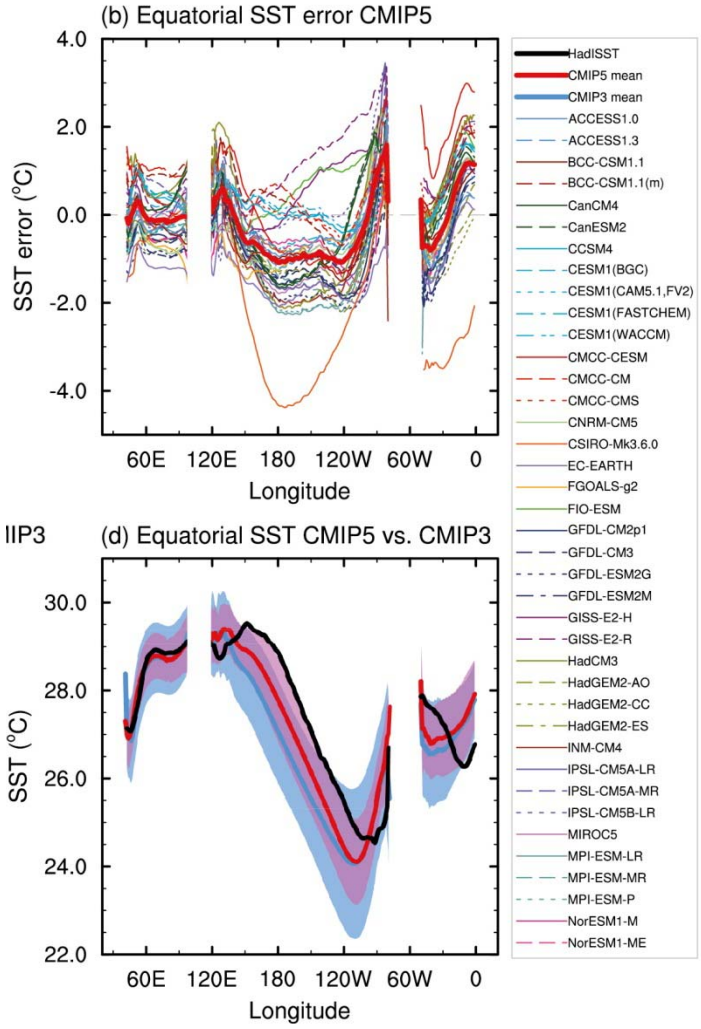

Figure 7. Annual-mean SST climatology at the equator. (lower panel) Comparison of Coupled Model Intercomparison Project phases 3 and 5 (CMIP3 & 5) and observations. (upper) Model errors. Figure 9.14 from [14]. These errors in SST are closely related to errors in wind forced divergence of surface currents.

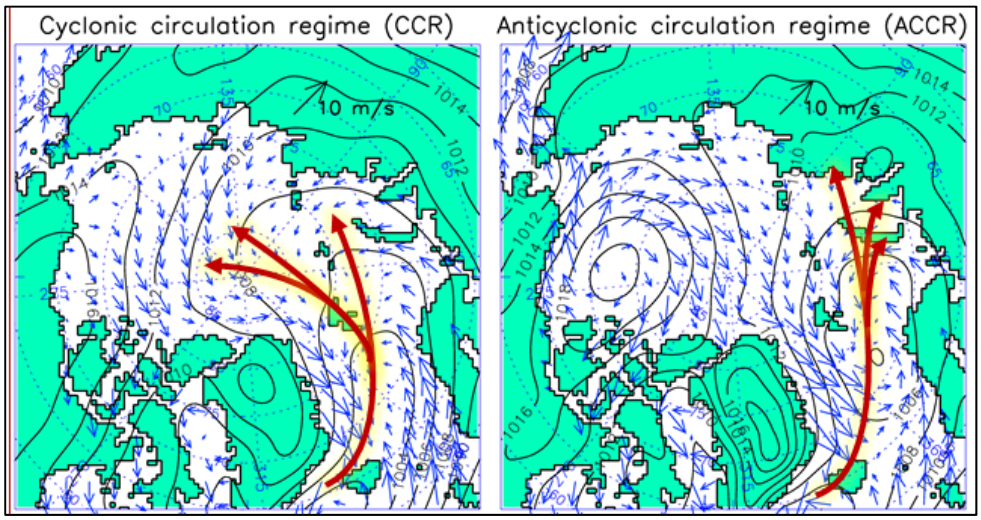

Figure 8: The panels show typical annual distributions of Sea Level Pressure and surface winds for cyclonic and anticyclonic atmospheric circulation regimes, respectively; red arrows show prevailing cyclone tracks (from [22]). The Arctic climate oscillates between the anticyclonic and cyclonic regimes described in terms of the Arctic Ocean Oscillations [69]. The index is a measure of the intensity and sense (clockwise/anticyclonic or counterclockwise/cyclonic) of the Arctic Ocean wind-driven sea ice and upper ocean circulations. During a `cyclonic regime, low SLP dominates over the central Arctic Ocean (left), with winds forcing the sea ice to drift cyclonically. Both exports of sea ice and low salinity polar water to Nordic Seas increase [69; 21]. Anomalously high freshwater flux results in freshening of the upper Nordic Seas. The Great Salinity Anomalies (GSAs) observed in the North Atlantic Subpolar Region in the 1970s, 1980s and 1990s correlate well with the history of the advent of cyclonic regimes starting several years after the initiation of cyclonic regimes over the Arctic Ocean. By contrast, during an anticyclonic regime (right), the trajectories of North Atlantic cyclones are shifted eastward resulting in fewer cyclones reaching the central Arctic. In this climate regime, high SLP dominates over the Arctic with anticyclonic winds forcing sea ice to drift clockwise. During a typical anticyclonic regime, the Arctic atmosphere is relatively cool and dry. Lower-than-normal air temperatures and anticyclonic winds lead to thicker ice and increased ice extent compared with a cyclonic regime. During an anticyclonic regime, freshwater is accumulated in the Beaufort Gyre of the Canada Basin due to Ekman transport convergence, reducing freshwater transport towards the Subpolar North Atlantic (which includes the Labrador Sea and Nordic Seas). This could lead to reduced stratification of the upper ocean there, promoting deep convection and atmospheric warming

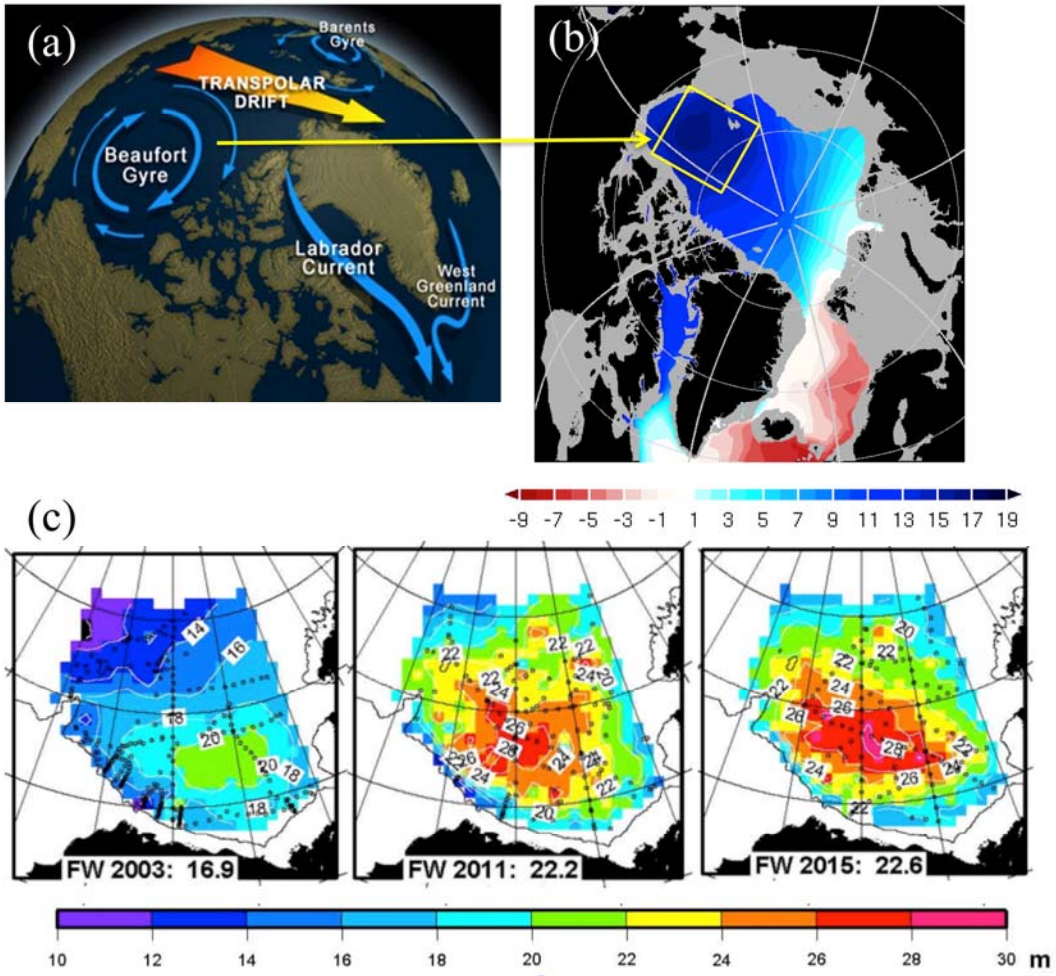

Figure 9: (a) Schematic of the major upper-ocean currents in the Arctic Ocean and Subpolar North Atlantic (figure source: 70). The Beaufort Gyre is the wind-driven anticyclonic vortex that accumulates liquid freshwater and sea ice as a result of convergent flows. (b) Freshwater content (m) in the Arctic Ocean and the Subpolar North Atlantic calculated from the Generalized Digital Environment Model (GDEM-V 3.0) climatology (reference salinity 34.8). Negative values indicate the freshwater deficit in the region relative to the reference salinity. The largest freshwater content is in the Beaufort Gyre region. (c) Change of the freshwater content in the Beaufort Gyre from Beaufort Gyre Observing System observational data (23, updated). The freshwater content in the region has been steadily increasing during the 21st century.

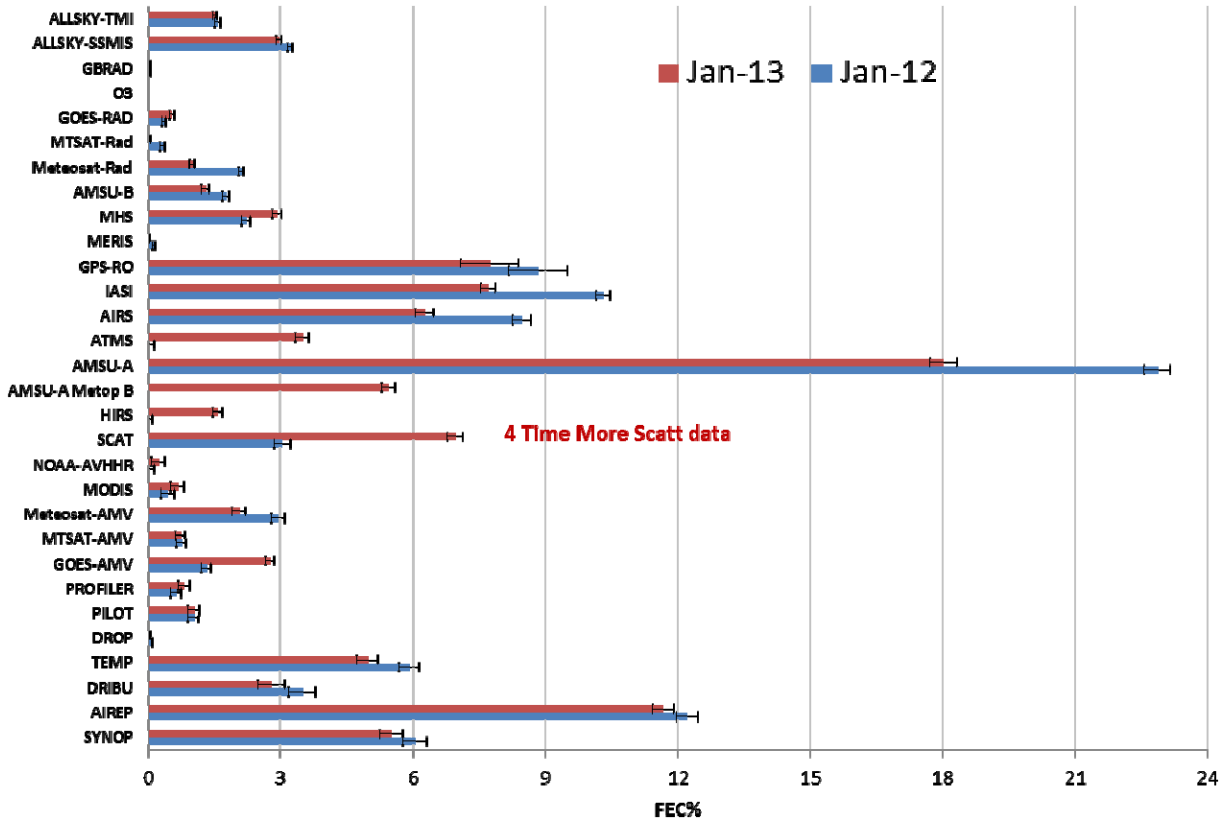

Fig. 10: Impacts on ECMWF Short-term (24 hour) Forecasts Error Reduction. The European Center for Medium-range Weather Forecast's (ECMWF) forecast sensitivity tool computes the Forecast Error Contribution (FEC) that is a measure (%) of the variation of the forecast error (as defined through the dry energy norm) due to the assimilated observations. This graphic, from [71], focuses on reduction of error. Only one scatterometer was assimilated in Jan. 2012. In Jan., 2013 two additional scatterometers, one with the full wide swath coverage similar to QuikSCAT were assimilated. Adding one wide-swath scatterometer has a large impact on forecasts.

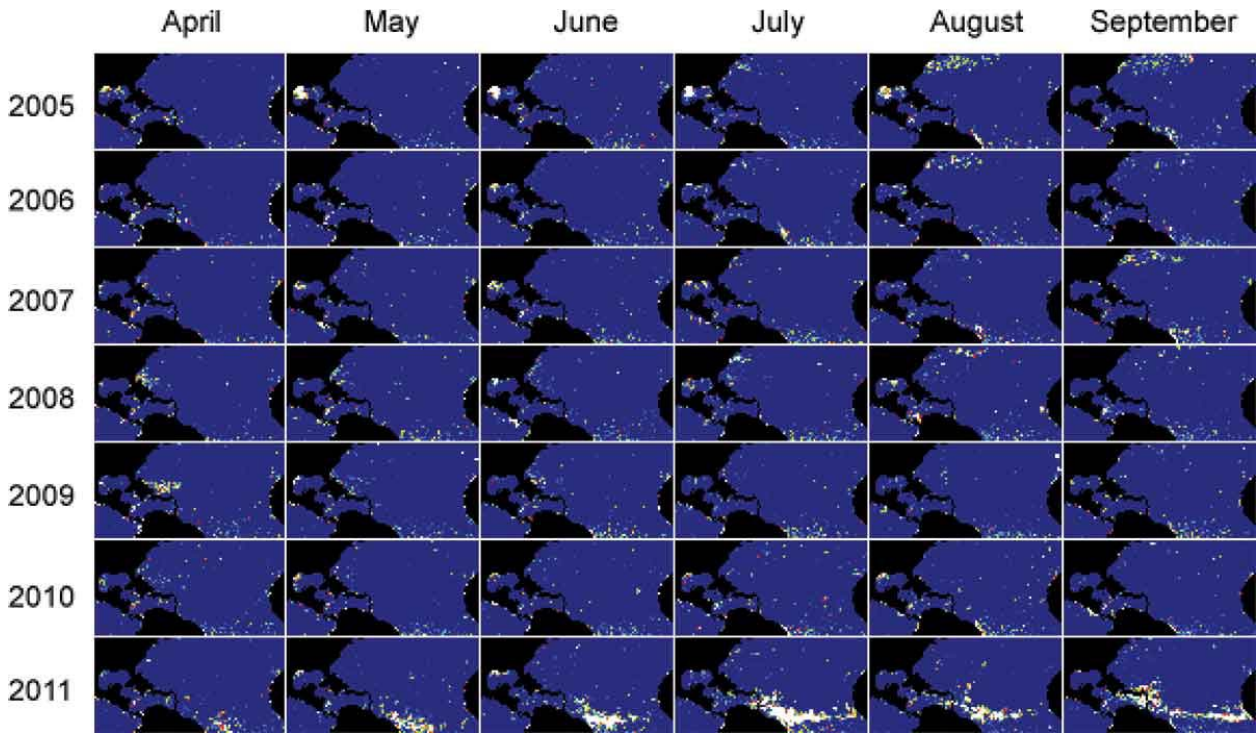

Figure 11: Monthly time series of MERIS Maximum Chlrophyll Index (MCI), an indicator of *Sargassum* slicks. An anomalous concentration of *Sargassum* was observed in the Caribbean in 2011. These time series suggest that this *Sargassum* may have been advected from the area near the Amazon River. In contrast, an anomalous concentration in the western Gulf of Mexico in 2005 appears to have originated locally. Given measurements of the currents very near the ocean surface at daily or more frequent sampling, the origins and pathways of such anomalous ecological events can be traced through Lagrangian analysis. Image reproduced from [32].

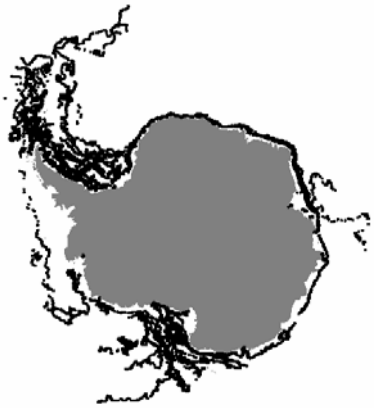

Figure 12: (left) Photos of several Antarctic tabular icebergs. Such icebergs are formed by calving off of major ice sheets fed by glaciers. The vertical height above the surface is 30 m with a total thickness of up to 300 m. The largest iceberg observed was 60 by 183 nautical miles in size. (right) Plotted daily positions of Antarctic tabular icebergs from 10 years of scatterometer data from the Scatterometer Climate Record Pathfinder (www.scp.byu.edu). There is a strong CCW transport of icebergs from the Ross Sea (at the bottom) around the Antarctic continent (in grey) near the coast. (The overlapping tracks hide the number of iceberg tracks shown here, which exceeds 100.) More 95% of all Antarctic icebergs are transported through the Weddell Sea (at the upper left of the image) regardless of their origin [67].

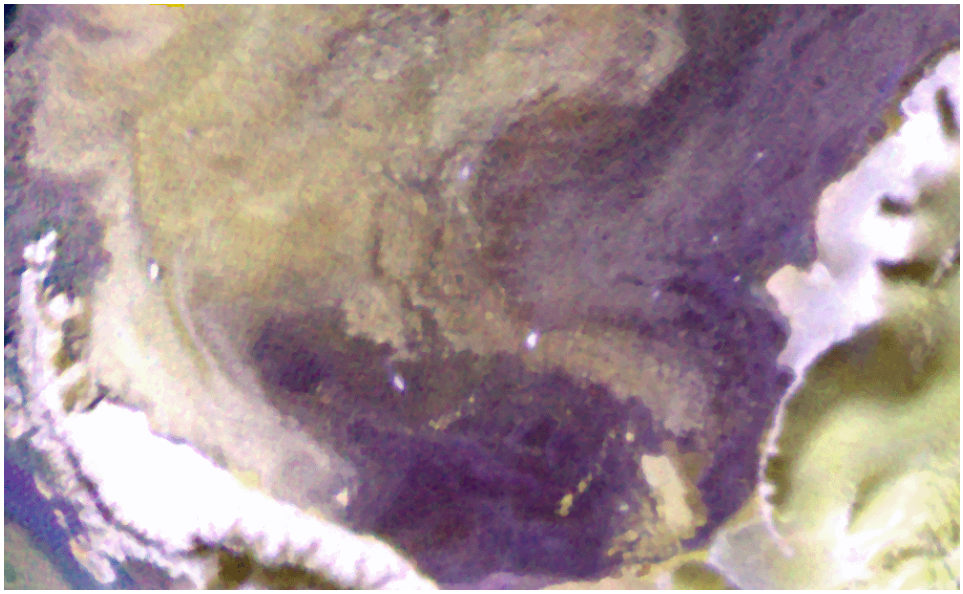

Figure 13: Colorized image of scatterometer-derived backscatter from a single day of data from the Ku-band QuikSCAT scatterometer (red=H pol, green=V pol) and the C-band ASCAT scatterometer (blue=V pol) showing the Weddell Sea. The resolution is 2.225 km per pixel. Ice sheets and icebergs show up as white, while glaciated regions over land and multi-year sea ice are gold-colored. First-year sea ice is purple colored. A small patch of open ocean off the East coast of the Antarctic Peninsula is blue. Note the number of icebergs present that are visible as white patches in the sea ice. Some icebergs are in gold left of center in the bottom of the image.

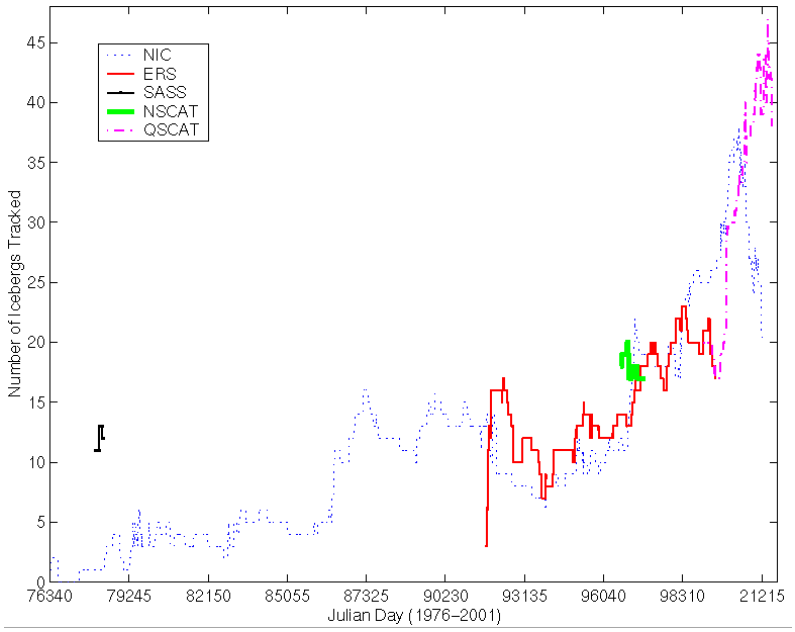

Figure 14: A plot of the number of Antarctic icebergs being tracked by the U.S. National Ice Center (NIC) and from scatterometer data by researchers using scatterometer data versus time from 1978 through 2001. The various scatterometers in the legend are: the European Remote Sensing Satellite (ERS) [1992-2000], the U.S. Seasat Satterometer (SASS) [1978], the NASA scatterometer (NSCAT) [1996-1997], and the QuikSCAT satterometer (QSAT) [1999-present]. This time series continues to the present with addition of the European ASCAT and Indian OSCAT sensors. Note that the NIC significantly undercounted icebergs prior to 1986, but became more accurate later, in part because they began using QuikSCAT data. The strong rise in the number of icebergs after 1999 is the result of two major calving events from the Ross Iceshelf [68].

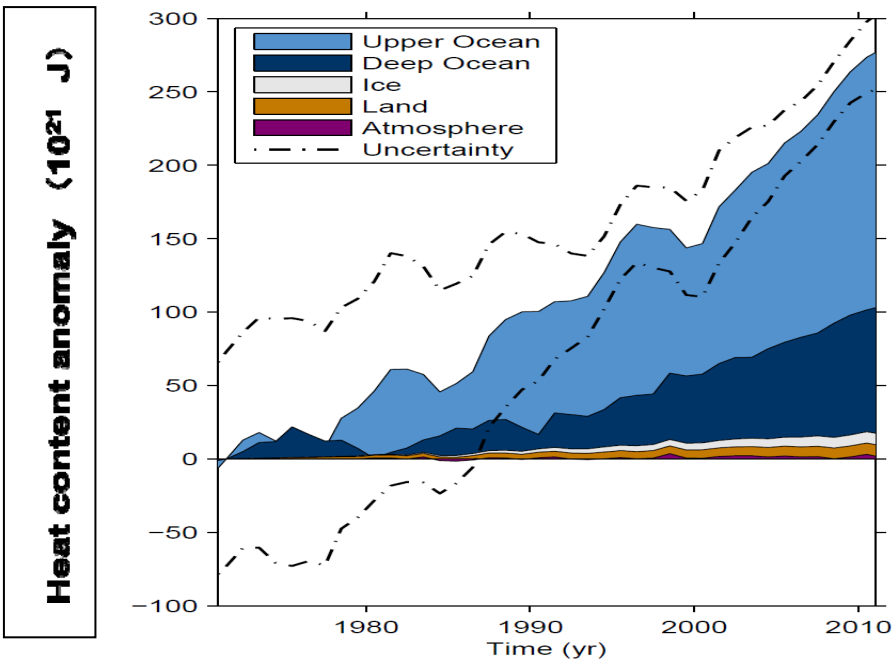

Figure 15: Time series of the change in heat content of the Earth system, showing the evolving change in storage in the upper ocean (upper 700m), deeper ocean, ice, land and atmosphere. The dashed lines indicate uncertainty. 93% of the energy gained by the Earth system is going into the oceans. Graphic from IPCC [48].

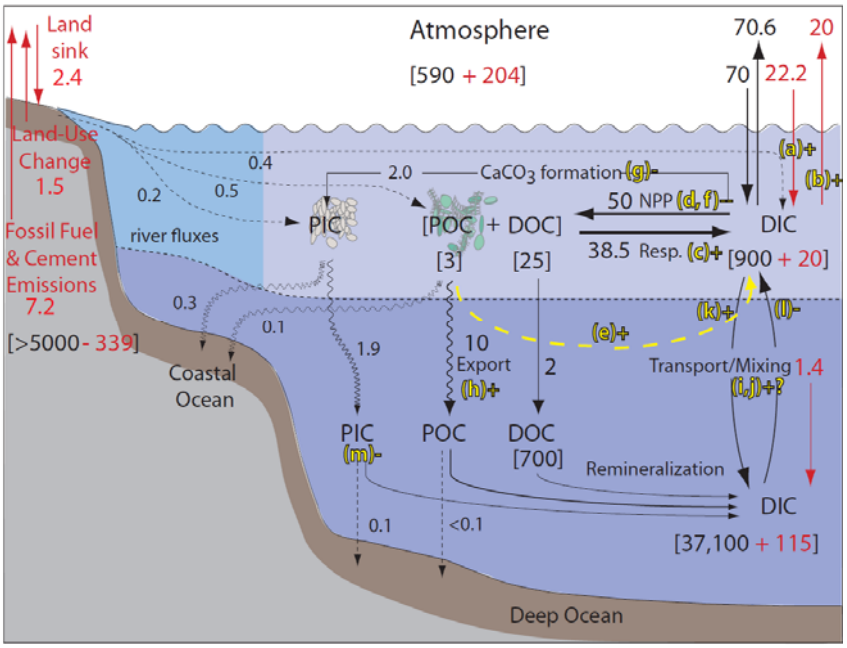

Figure 16: The ocean's Carbon cycle. Numbers in brackets are storages, and numbers without brackets are fluxes. Black is the estimated natural state and red is the anthropomorphic change. There are large regional differences. Flux Units of PgC/y (Petagram Carbon per year), sensitive to changes in surface stress and temperature. Graphic from [49].

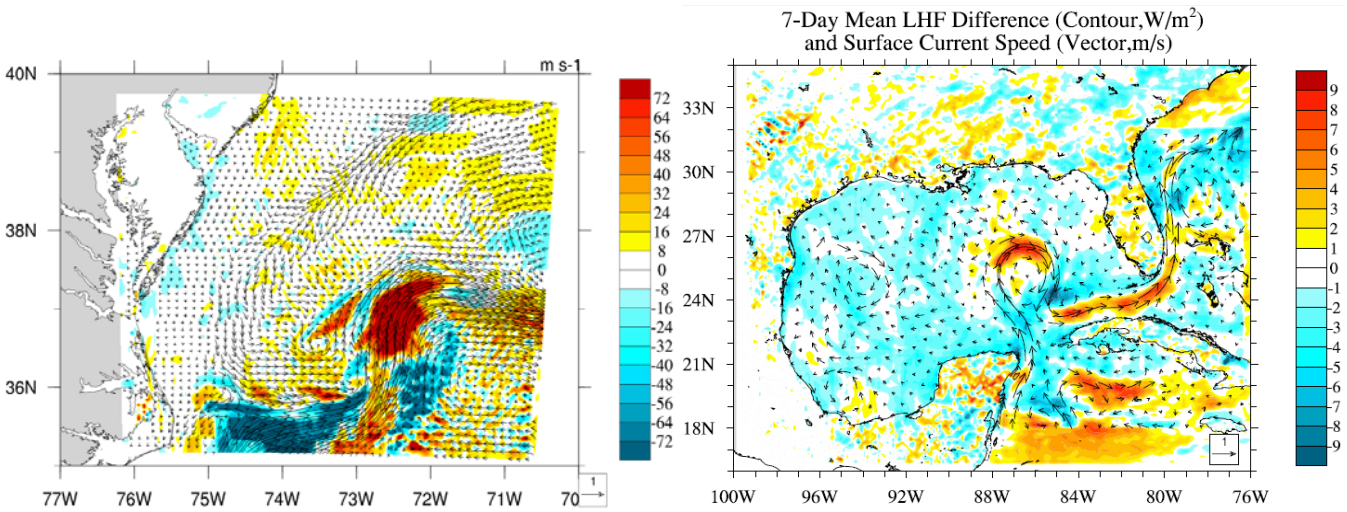

Figure 17: Example of surface currents impacting weather. The colors and heat fluxes and the vectors indicate the surface current direction and magnitude. The latent heat flux changes (left) in an extreme weather event: Hurricane Sandy (18 UTC Oct. 17, 2012 based on the Couple Ocean-Atmosphere-Wave-Sediment Transport (COAWST) model. These are modest compared to the total fluxes in the storm, but strong enough to have a large impact on the evolution of normal weather. A 14 day average of changes in latent heat flux due to currents in the Gulf of Mexico shows large changes over water as well as changes over land that are related to changes in boundary-layer height and precipitation. Graphics courtesy of Qi Shi.

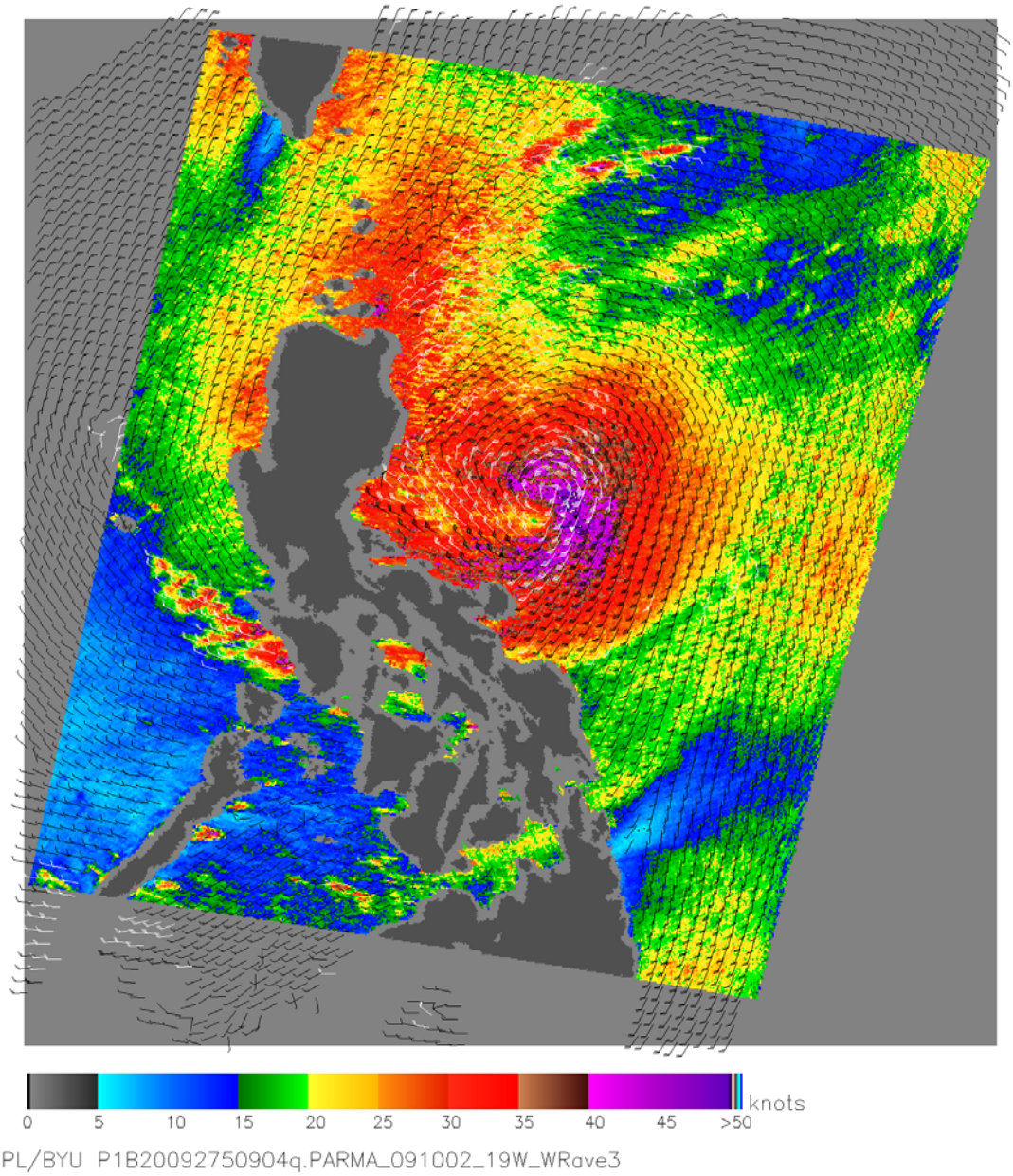

Figure 18: QuikSCAT observation of Typhoon Parma in 2009 just off the Philippines. The wind barb overlay shows the wind speed and direction field, while wind speed at UHR (2.5 km) is shown as the colored background. Note the fine detail, evidence of convective events and wind jets in island gaps. Such data is useful in studying cyclogenesis and predicting hazards. This image also illustrates that older scatterometers have had to mask larger areas near coastlines, removing data in a distance roughly equal to the width of one footprint. Much finer resolution, such as suggested herein, will result in data much closer to coastlines.

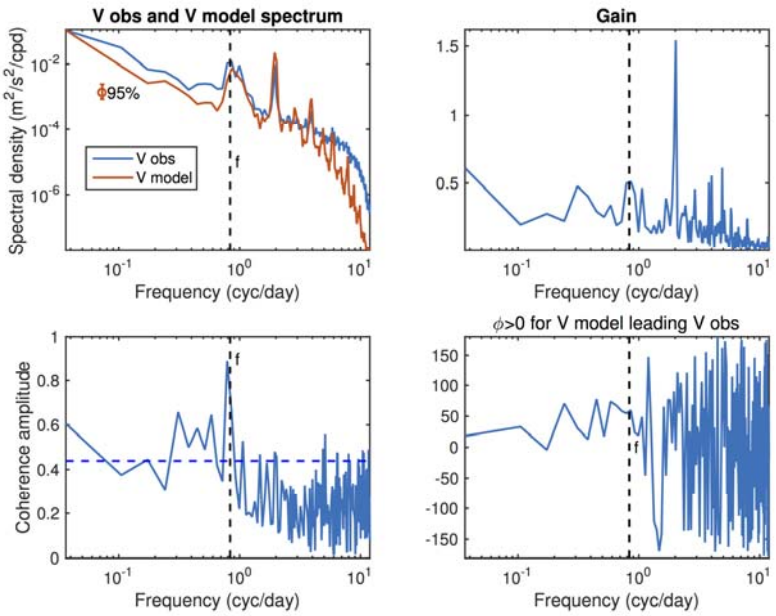

Figure 19 Spectral and cross-spectral comparison of surface currents from an internal-wave admitting global ocean simulation [45] driven by ECMWF atmospheric analysis and a time series of currents collected at 3.5-m depth from a moored buoy at 24.5N, 38W (subtropical Atlantic). The modeled and observed time series overlap for 219 days. The main point is that a global ocean model that was not specifically intended to accurately predict inertial currents produces a surface inertial current that is coherent with the observed inertial current (also true at other locations); this suggests that a global ocean model could be used to 'correct' satellite-measured surface currents to mitigate sampling errors associated with aliasing mixed-layer inertial oscillations. Upper-left panel: spectra of northward velocity component from the model (orange line) and the measurements (blue line). Lower-left panel: Coherence amplitude of the two time series, showing coherence in the inertial band is statistically different from zero at 95% confidence (significance level indicated by blue dashed line). Upper-right: Gain factor, showing that the coherent part of the model response has an amplitude that is about half as large as is observed. Lower-right: cross-spectral phase (we believe the phase shift at the inertial frequency is a result of a timing misalignment in the model forcing field).

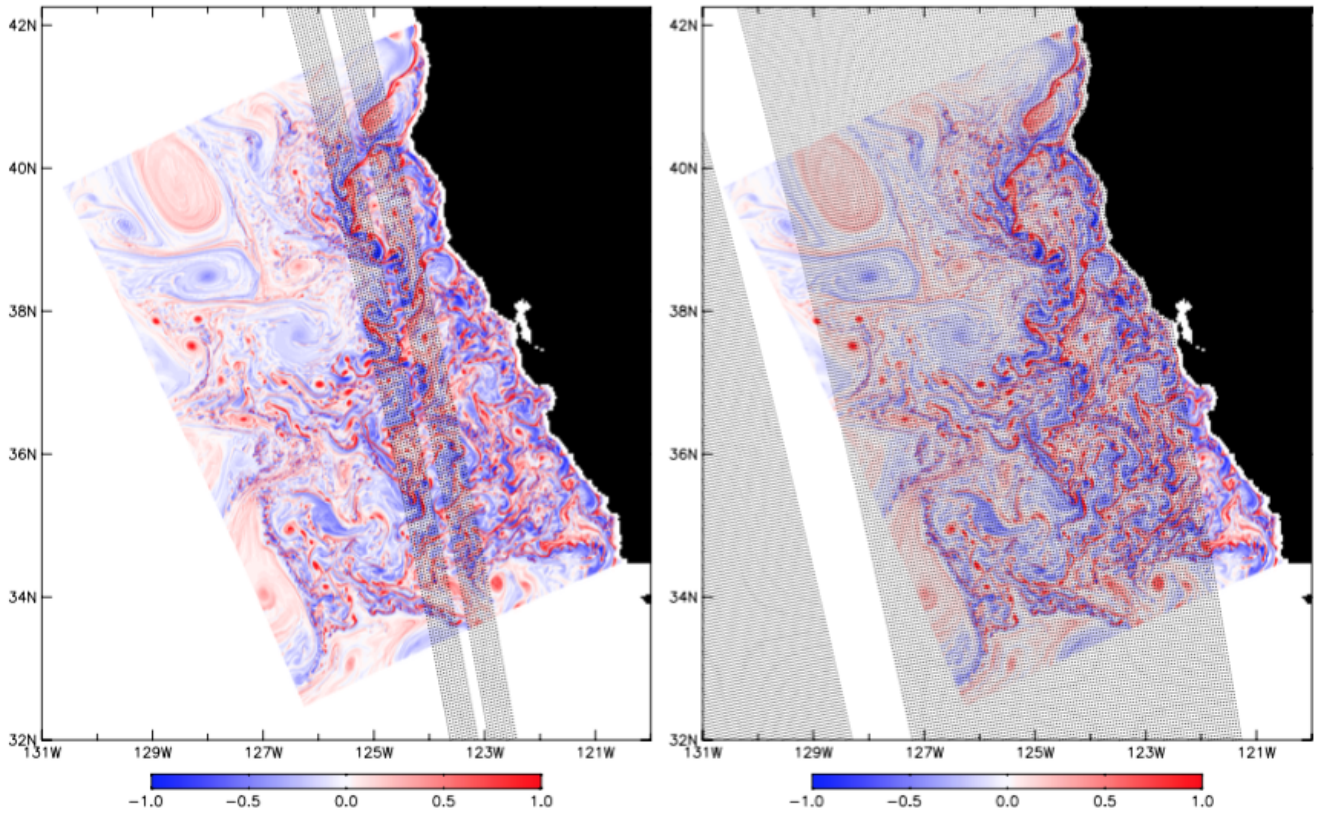

Figure [20]: Examples of the measurement swaths for single overpasses of the NASA SWOT mission (left) and half the swath of a wide-swath Doppler scatterometer system for the California Current (right).
:

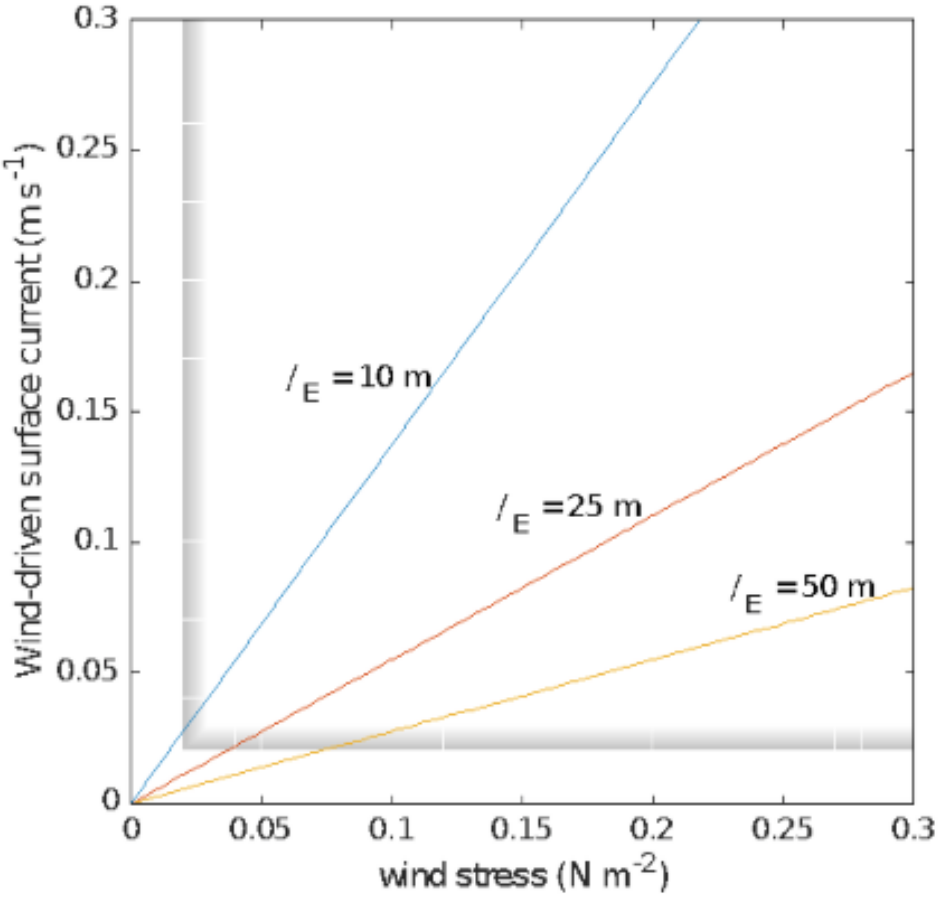

Figure 21: Illustration of the basis for technical requirements for wind stress and surface current, for the case in which the quantitative relation between wind stress and wind-driven, ageostrophic surface ocean current is estimated from classical Ekman theory for the ocean surface boundary layer. The linear, Ekman-theory dependence of surface ocean current on wind stress is shown for three typical ocean momentum boundary layer depths, l_E = {10, 25, 50} m, and surface wind stresses from 0 to 0.3 N m^{-2}. The associated theoretical Ekman surface current is directed at an angle of 45 degrees relative to the surface stress vector and ranges in magnitude from 0 to 0.3 m s^{-1} and. The shaded areas indicate the inferred nominal technical requirements for resolution of wind-driven surface currents for typical mid-ocean conditions ranging from moderately strong winds and moderately deep momentum boundary layers (stress = 0.1 N m^{-2}, l_E = 50 m) to weak winds and shallow boundary layers (stress = 0.02 N m^{-2}, l_E = 10 m).

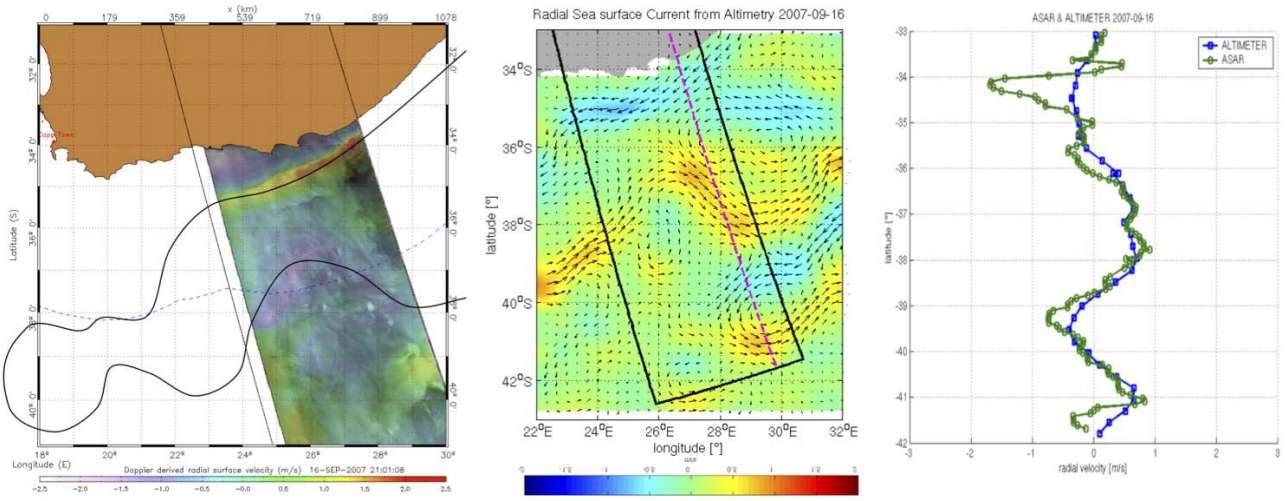

Figure 22: The left-most panel shows surface radial velocities (red is moving to the radar and blue away from the radar) measured by the ENVISAT SAR over the Aghulhas current region using Doppler techniques. The middle panel shows vector surface geostrophic currents estimated by a constellation of nadir altimeters in a merged product produced by AVISO. The black box corresponds to the SAR image and the red line to a cut displayed in the last panel. The last panel shows estimates of the radial current along the cut for the Doppler estimate (green) and the altimeter geostrophic current (blue). Notice that while there is general good agreement, the altimeter resolution is insufficient to resolve the narrow energetic Aghulhas current. [58]

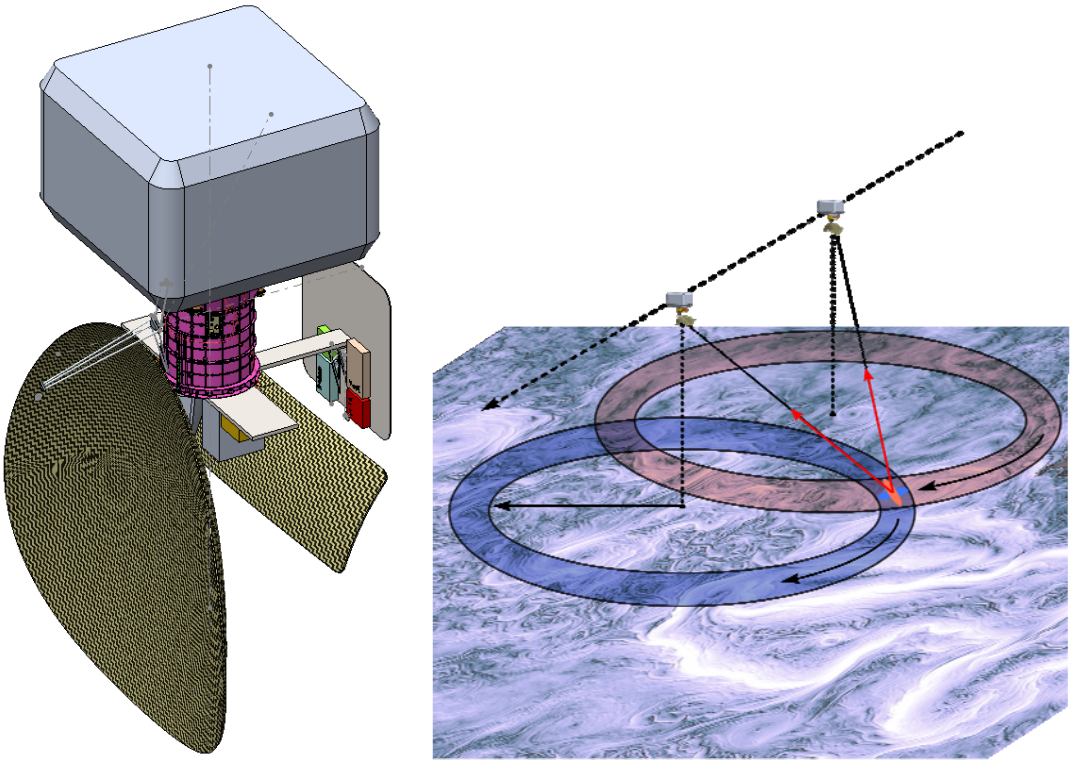

Figure 23: (left) Conceptual design for the Ku- and Ka-band Doppler scatterometer, studied by ISRO and JPL, mounted on the spacecraft bus. The larger of the two reflectors is Ku-band while the smaller is Ka-band. (right) Illustration of the Doppler scatterometer measurement concept. A rotating pencil beam illuminates a wide swath (~1600 km) at constant incidence angle, but different azimuth angles. By selecting the proper scan rate, each spot in the ground is illuminated at least twice with different azimuth angles, allowing vector wind and surface current estimation.